3D Numerical Simulation of Black Hole Formation Using Collisionless Particles
—— *Triplane Symmetric Case* ——

Masaru Shibata

Department of Earth and Space Science, Graduate School of Science
Osaka University, Toyonaka 560-0043, Japan

We have constructed a numerical code for 3D numerical relativity with which we can investigate black hole formation processes for a wide variety of problems. We adopt a standard 3+1 formalism for the evolution of geometric variables incorporating a swarm of collisionless particles as a source of the energy momentum tensor. In order to determine black hole formation, we also incorporate an apparent horizon finder which was recently developed. Assuming triplane symmetries with respect to x-y, y-z and z-x planes, we have performed a variety of simulations for black hole formation, such as the collapse of triaxial ellipsoids, collapse of spheroids of co-rotating and counter-rotating particles, and head-on collision of two nearly equilibrium spherical clusters, as well as test-bed simulations including spherical symmetric dust collapse. We present numerical results and demonstrate that using our numerical code, we can investigate black hole formation in these problems fairly accurately.

§1. Introduction

Numerical relativity plays two important roles in theoretical astrophysics and gravitational physics. One is to clarify formation processes of black holes (BHs). The reason is that the BH formation processes, such as stellar core collapse in the final phase of a massive star and coalescence of binary neutron stars and/or BHs should be common phenomena in our Universe, and that only by means of numerical relativity simulation, it is possible to perform experiments to gain theoretical understanding of such fully general relativistic phenomena occurring in nature. The other is to compute gravitational waveforms from such astrophysical phenomena. This comes from the fact that BH formation processes are also the most promising sources of gravitational radiation for planned kilometer size laser interferometric gravitational wave detectors such as LIGO,[1] VIRGO,[2] GEO[3] and TAMA.[4] In analyzing the signals of gravitational waves from such objects to extract a variety of information, we need theoretical templates of gravitational waveforms from the formation processes of BHs, because by comparing the templates it will be possible to extract a physical information from a signal of gravitational waves.

Since the general relativistic phenomena cited above generally occur in a non-axisymmetric manner, we need 3D numerical relativity simulations. However, in order to make it possible to perform such simulations, there are many questions at issue for 3D numerical relativity. We now list some of the questions:
- What is a formalism that allows stable numerical evolution?
- What are appropriate slice and spatial gauge conditions?

- What is a good method for finding the apparent horizon which is utilized for determining BH formation?
- What is an appropriate wave extraction method to analyze gravitational waves?
- What are appropriate boundary conditions at outer boundaries of numerical grids to avoid spurious backscattering of waves, numerical instability caused by incorrect boundary conditions, and so on?
- How should we treat a region near a BH horizon in which the gradient of the geometric variables is very steep?

To obtain a reliable result for the formation of BHs and computation of gravitational waves in 3D numerical relativity simulations, we must resolve all of these problems. In the past years, considerable effort has been devoted by several groups to find answer to these questions and much progress has been made.[5] However, we are still on the way to the goal. In this paper, we present the first result of our recent effort toward this goal, paying particular attention to formation processes of BHs.

In order to investigate BH formation as well as to find answers to the above questions, we have developed a numerical simulation code in which we adopt a 3+1 formalism for evolution of geometric variables,[6] incorporating a swarm of collisionless particles as a source of the energy momentum tensor and an apparent horizon finder which was recently developed for determining BH formation.[7] Using this code, we have performed many numerical simulations of BH formation in a variety of problems. We show that our present scheme is appropriate for the investigation of formation processes of BHs for several types of problems.

A feature of this work is that we use a swarm of collisionless particles as a source of the energy momentum tensor. The motivation is simple: As Shapiro and Teukolsky have often stated,[8] working with collisionless particles has several advantages over fluid systems for performing numerical relativity. Equations for collisionless particles are the geodesic equations (i.e., ordinary geodesic equations) while hydrodynamic equations are partial differential equations. Hence, the equations are much more tractable in numerical work, and we can focus most of the computational effort on solving Einstein field equations for geometric variables and resolving the problems described above such as a choice of gauge conditions, construction of an accurate apparent horizon finder, and so on.

The paper is organized as follows. In §2, we give the basic equations to be solved in the numerical simulations. In §3, we specify the gauge conditions which we adopt in this paper. In §4, we briefly explain the equation for determining the apparent horizon and a numerical method for finding it. In §5, we describe equations and methods to give initial conditions. In particular, we present a simple method for obtaining analytic solutions of the extrinsic curvature in solving the momentum constraint equation. In §6, the numerical methods and boundary conditions we adopt in this paper are summarized. In §7, we demonstrate that our numerical code can correctly generate exact (or nearly exact) solutions, such as spherical symmetric dust collapse and evolution of Teukolsky linear gravitational waves.[9] In §8, we give numerical results on formation processes of BHs in triaxial collapse, spheroidal collapses of co-rotating and counter-rotating particles with no net angular momentum, and head-on collisions of two boosting clusters. We show that our present scheme is

appropriate for the investigation of the BH formation process. Section 9 is devoted to discussion.

Throughout this paper, we adopt units in which $G = 1 = c$. Latin and Greek indices denote spatial components (1–3) and spacetime components (0–3), respectively. As spatial coordinates, we use the Cartesian coordinates $x^k = (x, y, z)$ with $r \equiv \sqrt{x^2 + y^2 + z^2}$.

§2.   Basic equations

We solve the Einstein equation using the 3+1 formalism in general relativity. The line element is written as

$$
\begin{aligned}
ds^2 &= g_{\mu\nu}dx^\mu dx^\nu \\
&= (-\alpha^2 + \beta_k \beta^k)dt^2 + 2\beta_i dx^i dt + \gamma_{ij}dx^i dx^j,
\end{aligned} \tag{2·1}
$$

where $g_{\mu\nu}$, α, β^i ($\beta_i = \gamma_{ij}\beta^j$), and γ_{ij} are the 4D metric, lapse function, shift vector, and 3D spatial metric, respectively. Because we use these in numerical simulations, we define the quantities

$$
\gamma = \det(\gamma_{ij}) \equiv e^{12\phi}, \tag{2·2}
$$

$$
\tilde{\gamma}_{ij} \equiv e^{-4\phi}\gamma_{ij}, \text{ i.e., } \det(\tilde{\gamma}_{ij}) = 1, \tag{2·3}
$$

$$
\tilde{A}_{ij} \equiv e^{-4\phi}\left(K_{ij} - \frac{1}{3}\gamma_{ij}K\right), \tag{2·4}
$$

where K_{ij} is the extrinsic curvature, and $K = K_k{}^k$. We note that indices of $\tilde{A}_{ij}$ and/or $\tilde{A}^{ij}$ are raised and lowered in terms of $\tilde{\gamma}_{ij}$ and $\tilde{\gamma}^{ij}$. In numerical computation, we solve for $\tilde{\gamma}_{ij}$, $\tilde{A}_{ij}$, ϕ and K instead of γ_{ij} and K_{ij}. Hereafter, we use ∇_μ, D_i and $\tilde{D}_i$ as the covariant derivatives with respect to $g_{\mu\nu}$, γ_{ij} and $\tilde{\gamma}_{ij}$, respectively.

As a source of the energy momentum tensor, we consider a swarm of collisionless particles. In this case, the energy momentum tensor is written as [10]

$$
T_{\mu\nu} = \sum_{a=1}^{N} m_a \frac{\delta^{(3)}(x^j - x_a^j)}{\alpha e^{6\phi}} \left(\frac{u_\mu u_\nu}{u^0}\right)_a, \tag{2·5}
$$

where m_a and x_a^j are the rest mass and the position of one of the particles, N is the total particle number, u_μ is the four-velocity of a particle, and $\delta^{(3)}(x^j - x_a^j)$ is a delta function in 3D spatial hypersurface. Note that the rest mass density ρ_* and the total rest mass (i.e., conserved mass) M_* are written as

$$
\rho_* = \sum_{a=1}^{N} m_a \delta^{(3)}(x^j - x_a^j), \tag{2·6}
$$

$$
M_* = 8\sum_{a=1}^{N} m_a, \tag{2·7}
$$

where the factor 8 in Eq. (2·7) arises because we assume triplane symmetries with respect to x-y, y-z and z-x planes in this paper.

The equation of motion for a particle is the geodesic equation

$$u^\mu \nabla_\mu u_\nu = 0. \tag{2.8}$$

The explicit form for the spatial component is written as

$$\frac{du_i}{dt} = -\alpha u^0 \alpha_{,i} + u_j \beta^j{}_{,i} - \frac{u_j u_k}{2u^0} \gamma^{jk}{}_{,i}. \tag{2.9}$$

Once u_i is obtained, u^0 is determined from the normalization relation of the four-velocity,

$$(\alpha u^0)^2 = 1 + \gamma^{ij} u_i u_j. \tag{2.10}$$

Note that the relation between the coordinate-based velocity $dx^i/dt \equiv u^i/u^0$ and u_j is

$$\frac{dx^i}{dt} = -\beta^i + \frac{\gamma^{ij} u_j}{u^0}. \tag{2.11}$$

Equations (2.9) and (2.11) constitute basic equations for the evolution of particle positions.

The Einstein equation is split into the constraint and evolution equations. The Hamiltonian and momentum constraint equations are

$$R - \tilde{A}_{ij}\tilde{A}^{ij} + \frac{2}{3}K^2 = 16\pi E, \tag{2.12}$$

$$D_i \tilde{A}^i{}_j - \frac{2}{3}D_j K = 8\pi J_j, \tag{2.13}$$

where

$$E = \sum_{a=1}^{N} m_a u_a^0 \alpha e^{-6\phi} \delta^{(3)}(x^k - x_a^k), \tag{2.14}$$

$$J_i = \sum_{a=1}^{N} m_a (u_i)_a e^{-6\phi} \delta^{(3)}(x^k - x_a^k), \tag{2.15}$$

and R is the scalar curvature with respect to γ_{ij}.

Following a previous work, we write evolution equations for geometric variables as follows: [6]

$$(\partial_t - \beta^k \partial_k)\tilde{\gamma}_{ij} = -2\alpha \tilde{A}_{ij} + \tilde{\gamma}_{ik}\beta^k{}_{,j} + \tilde{\gamma}_{jk}\beta^k{}_{,i} - \frac{2}{3}\tilde{\gamma}_{ij}\beta^k{}_{,k}, \tag{2.16}$$

$$(\partial_t - \beta^k \partial_k)\tilde{A}_{ij} = e^{-4\phi}\left[\alpha\left(R_{ij} - \frac{1}{3}\gamma_{ij}R\right) - \left(D_i D_j \alpha - \frac{1}{3}\gamma_{ij}D_k D^k \alpha\right)\right]$$
$$+ \alpha(K\tilde{A}_{ij} - 2\tilde{A}_{ik}\tilde{A}_j{}^k) + \beta^k{}_{,i}\tilde{A}_{kj} + \beta^k{}_{,j}\tilde{A}_{ki} - \frac{2}{3}\beta^k{}_{,k}\tilde{A}_{ij}$$
$$- 8\pi\alpha e^{-4\phi}\left(S_{ij} - \frac{1}{3}\gamma_{ij}S_k{}^k\right), \tag{2.17}$$

$$(\partial_t - \beta^k \partial_k)\phi = \frac{1}{6}\left(-\alpha K + \beta^k{}_{,k}\right), \tag{2.18}$$

$$(\partial_t - \beta^k \partial_k)K = \alpha\left(\tilde{A}_{ij}\tilde{A}^{ij} + \frac{1}{3}K^2\right) - D_k D^k \alpha + 4\pi\alpha(E + S_k{}^k), \tag{2.19}$$

where R_{ij} is the Ricci tensor with respect to γ_{ij}, and

$$S_{ij} = \sum_{a=1}^{N} m_a \left(\frac{u_i u_j}{u^0} \right)_a \frac{\delta^{(3)}(x^k - x_a^k)}{\alpha e^{6\phi}}. \tag{2·20}$$

To evaluate R_{ij} in Eq. (2·17), we use a technique employed in a previous work. [6] First, we split R_{ij} as

$$R_{ij} = \tilde{R}_{ij} + R_{ij}^{\phi}, \tag{2·21}$$

where $\tilde{R}_{ij}$ is the Ricci tensor with respect to $\tilde{\gamma}_{ij}$ (which does not depend on ϕ), and

$$R_{ij}^{\phi} = -2\tilde{D}_i\tilde{D}_j\phi - 2\tilde{\gamma}_{ij}\tilde{D}_k\tilde{D}^k\phi + 4\tilde{D}_i\phi\tilde{D}_j\phi - 4\tilde{\gamma}_{ij}\tilde{D}_k\phi\tilde{D}^k\phi. \tag{2·22}$$

For evaluation of $\tilde{R}_{ij}$, we introduce the new variable $F_i \equiv \delta^{jl}\tilde{\gamma}_{ij,l}$, where $\delta_{jl} = \delta^{jl}$ denotes the Kronecker delta. Then, using the property $\det(\tilde{\gamma}_{ij}) = 1$, $\tilde{R}_{ij}$ can be written as

$$\tilde{R}_{ij} = \frac{1}{2}\left[-\delta^{kl}h_{ij,kl} + F_{i,j} + F_{j,i} + f^{kl}(h_{lj,ik} + h_{li,jk} - h_{ij,kl}) \right.$$
$$\left. + f^{lk}{}_{,k}(h_{lj,i} + h_{li,j} - h_{ij,l}) \right] - \tilde{\Gamma}_{kj}^l\tilde{\Gamma}_{li}^k, \tag{2·23}$$

where $h_{ij} = \tilde{\gamma}_{ij} - \delta_{ij}$, $f^{ij} = \tilde{\gamma}^{ij} - \delta^{ij}$ and $\tilde{\Gamma}_{ij}^k$ is the Christoffel symbol with respect to $\tilde{\gamma}_{ij}$.

The equation for F_i is derived by operating on Eq. (2·16) with $\delta^{jl}\partial_l$ as

$$(\partial_t - \beta^k\partial_k)F_i = 2\alpha\left(f^{kj}\tilde{A}_{ik,j} + f^{kj}{}_{,j}\tilde{A}_{ik} - \frac{1}{2}\tilde{A}^{jl}h_{lj,i} + 6\phi_{,k}\tilde{A}^k{}_i - \frac{2}{3}K_{,i} \right)$$
$$- 2\delta^{jk}\alpha_{,k}\tilde{A}_{ij} + \delta^{jl}\beta^k{}_{,l}h_{ij,k} + \left(\tilde{\gamma}_{il}\beta^l{}_{,j} + \tilde{\gamma}_{jl}\beta^l{}_{,i} - \frac{2}{3}\tilde{\gamma}_{ij}\beta^l{}_{,l} \right)_{,k}\delta^{jk}$$
$$- 16\pi\alpha J_i, \tag{2·24}$$

where we have used the equation of the momentum constraint to rewrite the right-hand side. As we mentioned in a previous paper, [6] introduction of F_i for calculation of $\tilde{R}_{ij}$ is an important element in order to maintain stability in numerical simulation.

The choice of the method for computation of R in Eq. (2·17) is also critical. We have two options for the computation. One is that we use the Hamiltonian constraint, i.e., $R = 16\pi E + \tilde{A}_{ij}\tilde{A}^{ij} - 2K^2/3$. The other is to calculate the trace of R_{ij} directly. In the former case, if the Hamiltonian constraint holds exactly at all times, the trace of $R_{ij} - \gamma_{ij}R/3$ remains zero. However, if this is not the case due to numerical error, the trace of $\tilde{A}_{ij}$ deviates from zero gradually, and consequently, $\det(\tilde{\gamma}_{ij})$ deviates from unity. In numerical computation, the Hamiltonian constraint holds *approximately*, but not exactly. This causes the violation of the traceless property $\tilde{A}_{ij}\tilde{\gamma}^{ij} = 0$. To avoid this pathological feature, we use the latter method to estimate R; i.e., we calculate it as

$$R = e^{-4\phi}\tilde{\gamma}^{ij}(\tilde{R}_{ij} + R_{ij}^{\phi}). \tag{2·25}$$

More explicitly, we compute each element as

$$\tilde{\gamma}^{ij}\tilde{R}_{ij} = \frac{1}{2}\left[\delta^{kl}h_{ij,k}f^{ij}{}_{,l} + (F_{i,j} + F_{j,i})\tilde{\gamma}^{ij}\right.$$

$$+ \tilde{\gamma}^{ij}\{f^{kl}(h_{lj,ik} + h_{li,jk} - h_{ij,kl}) + f^{lk}{}_{,k}(h_{lj,i} + h_{li,j} - h_{ij,l})\}\Big]$$

$$- \tilde{\gamma}^{ij}\tilde{\Gamma}^l_{kj}\tilde{\Gamma}^k_{li}, \tag{2.26}$$

$$\tilde{\gamma}^{ij}R^\phi_{ij} = -8\tilde{D}_k\tilde{D}^k\phi - 8\tilde{D}_k\phi\tilde{D}^k\phi. \tag{2.27}$$

In this case, the traceless property of $R_{ij} - \gamma_{ij}R/3$ is guaranteed fairly precisely.

§3. Gauge conditions

The maximal slice condition, $K = 0 = \partial_t K$, is well-known because of its singularity avoidance property. In this condition, we obtain a Poisson type equation for α as

$$D_k D^k\alpha = 4\pi\alpha(E + S_k{}^k) + \alpha\tilde{A}_{ij}\tilde{A}^{ij}, \tag{3.1}$$

or

$$D_k D^k\ln\alpha + (D_k\ln\alpha)(D^k\ln\alpha) = 4\pi(E + S_k{}^k) + \tilde{A}_{ij}\tilde{A}^{ij}. \tag{3.2}$$

To impose the maximal slice condition, we need to solve the Poisson equation rigorously, but as it has been pointed out by many authors, the procedure is very time consuming. Thus, in this paper, we adopt an "approximate maximal slice condition" instead of a strict one; i.e., at each time step, we determine that α satisfies the maximal slice condition approximately. Our strategy is as follows: First, instead of Eq. (3.2), we construct a parabolic-type equation as

$$\partial_\lambda\ln\alpha = D_k D^k\ln\alpha + (D_k\ln\alpha)(D^k\ln\alpha)$$

$$- 4\pi(E + S_k{}^k) - \tilde{A}_{ij}\tilde{A}^{ij} - \frac{1}{3}K^2, \tag{3.3}$$

where λ is a parameter. The reason why we use this equation for $\ln\alpha$ instead of that of α is to guarantee the positivity of α. (As long as $\ln\alpha$ remains finite, α remains positive.) If we solve Eq. (3.3) for $\lambda \to \infty$ in each time slice, we will obtain a profile of α which satisfies the maximal slice condition. In our approximate maximal slice, at the n-th time step, we first set an initial profile of α by using α at the previous two time steps as

$$\alpha^{(n)} = (1 + f)\alpha^{(n-1)} - f\alpha^{(n-2)}, \tag{3.4}$$

where $\alpha^{(k)}$ denotes α at the k-th time step and f is a control parameter which we choose to be ~ 1. Then, $\ln\alpha$ evolves according to Eq. (3.3) to $\lambda = \lambda_0 \ll \infty$, where we take λ_0 as an appropriately large (but not too large) constant to give a new profile of α. (Note that at $t = 0$, we solve Eq. (3.1) exactly by using a Poisson solver (see §5).) Since we do not set $K = 0 = \partial_t K$ and do solve the evolution equation (2.19) of K for $t > 0$, K deviates from zero with time evolution in this method. However, the

deviation rate $\partial_t K$ can be kept small for an appropriate choice of λ_0. Consequently, α determined in this method is nearly identical with that determined by the maximal slice. This is actually the case for a spherically symmetric dust collapse, at least up to the formation of a BH, as we will demonstrate in §7.

As for the spatial gauge, it may be desirable to adopt a geometrically preferable condition, such as the minimal distortion gauge, [11] in which the global time rate of change in $\tilde{\gamma}_{ij}$ is minimized, suppressing the effect of the coordinate wave in $\tilde{\gamma}_{ij}$ as much as possible. However, to impose this condition, we need to solve a complicated vector Poisson-type equation, which is a very time consuming task. Since we guess that for problems in this paper, no serious troubles occur, we simply set $\beta^k = 0$. Appropriate choice of the spatial gauge condition is the subject in a subsequent paper. [12]

§4. Apparent horizon finder

The apparent horizon is defined as the marginally outermost trapped spacelike surface, and if it exists in the globally hyperbolic spacetime, it is guaranteed that the event horizon exists outside the apparent horizon, i.e., formation of a BH is guaranteed. [13] Thus, to investigate whether or not a BH is formed, searching for the apparent horizon on a 3D spatial hypersurface is a good method. Strictly speaking, we need to find the event horizon to make sure that BH formation takes place, because a BH may be formed if the apparent horizon is not formed in a 3D hypersurface. However, to determine the event horizon, it is necessary to keep all the data sets for the spacetime throughout the entire simulation, which is very difficult for present computers. In contrast, it is possible to determine if the apparent horizon exists only by examining a 3D hypersurface at each time step. This is the reason that the apparent horizon is a useful notion in numerical relativity.

If an apparent horizon exists, the following equation,

$$D_i s^i + K_{ij} s^i s^j - K = 0 \tag{4.1}$$

is satisfied on the closed spacelike two-surface. [15] Here s^i denotes a unit spacelike normal to the closed two-surface of the apparent horizon. Denoting the location of the apparent horizon as $r = h(\theta, \varphi)$, where θ and φ are angular coordinates, s_i can be expressed in the spherical coordinate as

$$s_i = \frac{e^{2\phi}}{C}(1, \ -h_{,\theta}, \ -h_{,\varphi}), \tag{4.2}$$

and

$$C = \left[\tilde{\gamma}^{rr} + \tilde{\gamma}^{\theta\theta}(h_{,\theta})^2 + \tilde{\gamma}^{\varphi\varphi}(h_{,\varphi})^2 - 2\tilde{\gamma}^{r\theta}h_{,\theta} - 2\tilde{\gamma}^{r\varphi}h_{,\varphi} + 2\tilde{\gamma}^{\theta\varphi}h_{,\theta}h_{,\varphi} \right]^{1/2}. \tag{4.3}$$

We note that in our numerical code of the apparent horizon finder, the spherical coordinate components of $\tilde{\gamma}^{ij}$ are used instead of the Cartesian coordinate components for convenience. This means that we perform a coordinate transformation from $\tilde{\gamma}^{xx}, \tilde{\gamma}^{xy}, \cdots$ to $\tilde{\gamma}^{rr}, \tilde{\gamma}^{r\theta}, \cdots$.

Substituting Eq. (4·2) into Eq. (4·1), we obtain a 2D Poisson-type equation as

$$h_{,\theta\theta} + \cot\theta h_{,\theta} + \frac{h_{,\varphi\varphi}}{\sin^2\theta} - 2h$$
$$= S(h, \theta, h_{,\theta}, h_{,\varphi}, h_{,\theta\theta}, h_{,\theta\varphi}, h_{,\varphi\varphi}, K_{ij}, \tilde{\gamma}^{ij}, \phi), \qquad (4\cdot4)$$

where S denotes a function. We solve this equation for a trial value of h as a boundary value problem, imposing the boundary conditions at $\theta = 0$, $\pi/2$ and $\varphi = 0$, $\pi/2$ as $h_{,\theta} = 0$ and $h_{,\varphi} = 0$, and continue the procedure iteratively until sufficient convergence for h is achieved. (See a previous paper [7] for a more detailed explanation of our numerical scheme.)

§5.   Initial conditions

Initial conditions are given by solving Eqs. (2·12) and (2·13). Hereafter, we consider the initial conditions of the conformal flat three metric (i.e., $\tilde{\gamma}_{ij} = \delta_{ij}$) and $K = 0$. Then, using the conformal factor $\psi = e^\phi$, $\hat{A}_{ij} = \psi^6 \tilde{A}_{ij}$ and $\hat{A}^{ij} = \psi^6 \tilde{A}^{ij}$, the Hamiltonian and momentum constraint equations are rewritten as

$$\Delta\psi = -2\pi E\psi^5 - \frac{1}{8}\hat{A}_{ij}\hat{A}^{ij}\psi^{-7}, \qquad (5\cdot1)$$

$$\hat{A}_i{}^j{}_{,j} = 8\pi J_i\psi^6, \qquad (5\cdot2)$$

where Δ denotes the Laplacian in the flat 3D space.

We first describe a method to find analytic solutions for $\hat{A}_{ij}$ for time-asymmetric initial conditions. We decompose $\hat{A}_{ij}$ as [7]

$$\hat{A}_{ij} = W_{i,j} + W_{j,i} - \frac{2}{3}\delta_{ij}W_{k,k}, \qquad (5\cdot3)$$

and using scalar and vector functions χ and B_i, we set W_i as

$$W_i = \frac{7}{8}B_i - \frac{1}{8}(\chi_{,i} + B_{k,i}x^k). \qquad (5\cdot4)$$

Then, the momentum constraint equation can be decomposed into two equations:

$$\Delta B_i = 8\pi J_i\psi^6,$$
$$\Delta\chi = -8\pi J_i x^i\psi^6. \qquad (5\cdot5)$$

We consider the case in which $u_i = u_i(\boldsymbol{r})$. In this case, we can set $J_i\psi^6 = \rho_* u_i$. To determine initial conditions, we first fix ρ_*, and then particles are appropriately distributed to construct the density profile.

First, we consider the case in which a cluster of particles is located around the origin, and attempt to find solutions for which ρ_* is given as the spherical symmetric function $f(r)$ and u_i is given as

$$u_i = \sum_{l,m} a_{i:l,m} Y_{l,m}(\theta, \varphi)r^l, \qquad (5\cdot6)$$

where $Y_{l,m}$ is a spherical harmonic function and $a_{i:l,m}$ is its coefficient. Then, B_i and χ are expressed using $Y_{l,m}$ and a radial function $\mathcal{Y}_l(r)$ that satisfies

$$\frac{1}{r^{l+2}}\frac{d}{dr}\left(r^{2l+2}\frac{d}{dr}\frac{\mathcal{Y}_l}{r^l}\right) = 4\pi f(r)r^l. \tag{5.7}$$

As a simple example, in this paper, we choose ρ_* to satisfy

$$\rho_* = f(r) = \begin{cases} \rho_0\left(1 - \dfrac{r^2}{r_o^2}\right)^2, & r < r_o, \\ 0, & r \geq r_o, \end{cases} \tag{5.8}$$

where ρ_0 and r_o are constants. Then,

$$\mathcal{Y}_l = \begin{cases} 4\pi\rho_0 r^l\left[\dfrac{r^2}{2(2l+3)} - \dfrac{r^4}{2(2l+5)r_o^2} + \dfrac{r^6}{6(2l+7)r_o^4} - \dfrac{r_o^2}{6(2l+1)}\right], & r \leq r_o, \\ -32\pi\rho_0 r_o^{2l+3}\dfrac{(2l-1)!!}{(2l+7)!!}\dfrac{1}{r^{l+1}}, & r \geq r_o. \end{cases} \tag{5.9}$$

Initial conditions for many clusters are easily constructed by summing up this solution. For example, if we wish to simulate a head-on collision of two clusters with a uniform boost velocity along the x-axis as

$$u_i = \left(-a\frac{|x|}{x},\ 0,\ 0\right), \tag{5.10}$$

where a is a positive constant, then we set the centers of the two clusters as $\boldsymbol{r}_c = (\pm x_c, 0, 0)$ and fix $\rho_* = f(|\boldsymbol{r}-\boldsymbol{r}_c|)+f(|\boldsymbol{r}+\boldsymbol{r}_c|)$. We then immediately obtain solutions for B_x and χ as

$$B_x = -2a[\mathcal{Y}_0(|\boldsymbol{r}-\boldsymbol{r}_c|) - \mathcal{Y}_0(|\boldsymbol{r}+\boldsymbol{r}_c|)], \tag{5.11}$$

$$\chi = 2a\left[\mathcal{Y}_1(|\boldsymbol{r}-\boldsymbol{r}_c|)\frac{x-x_c}{|\boldsymbol{r}-\boldsymbol{r}_c|} + x_c\mathcal{Y}_0(|\boldsymbol{r}-\boldsymbol{r}_c|)\right.$$
$$\left. -\mathcal{Y}_1(|\boldsymbol{r}+\boldsymbol{r}_c|)\frac{x+x_c}{|\boldsymbol{r}+\boldsymbol{r}_c|} + x_c\mathcal{Y}_0(|\boldsymbol{r}+\boldsymbol{r}_c|)\right], \tag{5.12}$$

and $B_y = B_z = 0$. If we wish to simulate a non-head-on collision between two clusters, for example, we choose the four-velocity

$$u_i = \left(0,\ a\frac{|x|}{x},\ 0\right), \tag{5.13}$$

where $a\ (>0)$ should be chosen to be smaller than the Kepler velocity for collision. Then, we obtain the solutions as

$$B_y = 2a[\mathcal{Y}_0(|\boldsymbol{r}-\boldsymbol{r}_c|) - \mathcal{Y}_0(|\boldsymbol{r}+\boldsymbol{r}_c|)], \tag{5.14}$$

$$\chi = -2a\left[\mathcal{Y}_1(|\boldsymbol{r}-\boldsymbol{r}_c|)\frac{y}{|\boldsymbol{r}-\boldsymbol{r}_c|} - \mathcal{Y}_1(|\boldsymbol{r}+\boldsymbol{r}_c|)\frac{y}{|\boldsymbol{r}+\boldsymbol{r}_c|}\right], \tag{5.15}$$

and $B_x = B_z = 0$. We can also give the initial condition for merging co-rotating two clusters using a similar procedure by setting $u_i = (-\Omega y, \Omega x, 0)$. In this way, using this method, it is very easy to give many types of simple initial conditions.

We note that Eqs. (5·10) and (5·13) do not always imply that all the particles in one cluster move homogeneously in one direction. For example, when we put equal numbers of co-rotating and counter-rotating particles at each point which still move coherently in the x-direction, the velocity field is expressed by Eq. (5·10). This means that it is possible to make not only collapsing clusters but also clusters in nearly equilibrium states using this simple method.

Once we obtain a solution for $\hat{A}_{ij}$, ψ is numerically computed by solving the Poisson equation (5·1) iteratively. In each iteration step, Eq. (5·1) is solved for a trial value of ψ determined in a previous step under the boundary condition at the outer boundaries

$$\psi = 1 + \frac{M}{2r} + O(r^{-3}), \tag{5·16}$$

where M is the gravitational mass calculated here as

$$M = \int dV \left(E\psi^5 + \frac{1}{16\pi\psi^7} \hat{A}_{ij} \hat{A}^{ij} \right). \tag{5·17}$$

The numerical method for solving the Poisson equation is the same as that used in a previous paper.[7] The iteration is repeated until sufficient convergence for ψ is achieved.

We also need to solve a Poisson-type equation for α in order to impose the maximal slice condition. On the conformal flat 3D space, the equation is written as [16]

$$\Delta(\alpha\psi) = 2\pi\alpha\psi^5(E + 2S_k{}^k) + \frac{7}{8}\alpha\psi^{-7}\hat{A}_{ij}\hat{A}^{ij}. \tag{5·18}$$

Hence, after we compute ψ, we can determine $\alpha\psi$ (and hence α) by using essentially the same method as that for solving ψ.

In the following, we consider three types of initial conditions. One is time-symmetric initial conditions with $u_i = 0$. In this case, we appropriately choose a non-spherical function for $\rho_* = E\psi^6$. In the second case, each particle is paired with another particle and we put the pair of particles at the same position. Then, we give co-rotating and counter-rotating angular velocities for each pair. Hence, there exist equal numbers of co-rotating and counter-rotating particles. Then, J_i is zero at each point, so that the initial hypersurface is time-symmetric, although u_i of each particle is not zero. In this case, we choose ρ_* simply as a spherical function. The third type of initial conditions is the time-asymmetric. In particular, in this paper, we consider head-on collisions of two clusters using the initial conditions given above.

§6. Numerical methods and boundary conditions

6.1. *Geometries*

In this paper, we assume triplane symmetries and solve equations in a single octant region (x, y, $z \geq 0$). Hence, we impose the reflection symmetric boundary

conditions on the $x = 0$, $y = 0$, and $z = 0$ planes.

At outer boundaries, we impose an outgoing wave boundary condition for h_{ij}, F_i, $\tilde{A}_{ij}$, [6]

$$rQ(u) = \text{const}, \tag{6·1}$$

where Q denotes one of the above quantities, and we choose u as

$$u = \alpha t - e^{2\phi} r \ . \tag{6·2}$$

More explicitly, Eq. (6·1) is rewritten as

$$Q(t,r) = \left(1 - \frac{\Delta r}{r}\right) Q(t - \Delta t, r - \Delta r), \tag{6·3}$$

where Δt is a time step, and $\Delta r = \alpha e^{-2\phi} \Delta t$. $Q(t - \Delta t, r - \Delta r)$ is linearly interpolated from the nearest 8 grid points.

For α and ϕ, we impose the following Neumann-type boundary conditions at the outer boundaries:

$$(r \ln \alpha)_{,r} = 0 \quad \text{and} \quad (r\phi)_{,r} = 0. \tag{6·4}$$

For K, we set simply $K = 0$ at outer boundaries.

Note that the above boundary conditions at outer boundaries are correct only approximately. This implies that small unphysical errors such as spurious back reflections of waves and excitations of unphysical waves will be generated in numerical simulations. To impose highly accurate boundary conditions will require a great deal of effort as has been demonstrated by several groups. [17] Imposing rigorous boundary conditions at outer boundaries is one of major unsolved problems in 3D numerical relativity.

In solving the evolution equations for geometric variables, we put $\tilde{\gamma}_{ij}$, F_i, ϕ and α on $t^{(0)}$, $t^{(1)}$, $t^{(2)} \cdots t^{(n)}$, and $\tilde{A}_{ij}$ and K on $t^{(1/2)}$, $t^{(3/2)} \cdots t^{(n+1/2)}$, where $t^{(k)}$ denotes the coordinate time at the k-th time step, and we use a leapfrog method to keep second order accuracy. Note that in the evolution equations, there are many terms which introduce first order errors (for example, α in Eqs. (2·16) and (2·18) and K^2 in Eq. (2·19).) We adjust for this problem by extrapolating the necessary variables to the $(n + 1/2)$ and $(n + 1)$ time slices, using at each grid point a formula such as

$$\alpha^{(n+1/2)} = \frac{3}{2}\alpha^{(n)} - \frac{1}{2}\alpha^{(n-1)},$$
$$K^{(n+1)} = \frac{3}{2}K^{(n+1/2)} - \frac{1}{2}K^{(n-1/2)}, \tag{6·5}$$

where $\alpha^{(k)}$ and $K^{(k)}$ denote α and K at the k-th time step. Then, second order accuracy in time is guaranteed. (Note that in the derivation of Eq. (6·5), we have implicitly assumed that the next two time steps $\Delta t^{(n)}$ and $\Delta t^{(n+1)}$ are approximately identical.) Since we also use a finite differencing of second order accuracy for the spatial derivative operators ∂_i and $\partial_i \partial_j$, second order accuracies in time and space are guaranteed for geometric variables in the present numerical simulations.

6.2. *Particles*

In the present numerical simulation, we use a particle mesh method for the evolution of the system. That is, geometric variables are represented approximately by values on grid points, and differential operators are replaced by finite difference approximations on the grid points. Geometric variables and their derivatives at the particle positions are obtained by interpolating the grid-defined values. Grid-defined matter densities, such as E, J_i and S_{ij}, are obtained by the opposite process of assigning the particle and its velocity attributes to nearby grid points in order to create the grid-defined values.

More concretely, we use the CIC scheme [14] for the interpolation. In the CIC scheme, values of geometric variables and their derivatives are interpolated from those on the nearest 8 grid points; i.e., if a particle stays at $\boldsymbol{r}_p = (x_p, y_p, z_p)$, where $x_i < x_p < x_{i+1}$, $y_j < y_p < y_{j+1}$, and $z_k < z_p < z_{k+1}$, then we interpolate the value of a variable Q at $\boldsymbol{r}_p$ as

$$
\begin{aligned}
[&\{f_x^+ Q_{i,j,k} + f_x^- Q_{i+1,j,k}\}f_y^+ \\
&+ \{f_x^+ Q_{i,j+1,k} + f_x^- Q_{i+1,j+1,k}\}f_y^-]f_z^+ \\
&+ [\{f_x^+ Q_{i,j,k+1} + f_x^- Q_{i+1,j,k+1}\}f_y^+ \\
&+ \{f_x^+ Q_{i,j+1,k+1} + f_x^- Q_{i+1,j+1,k+1}\}f_y^-]f_z^-\,,
\end{aligned} \tag{6·6}
$$

where $f_x^+ = (x_{i+1} - x_p)/\Delta x_i$, $f_x^- = 1 - f_x^+$, $f_y^+ = (y_{j+1} - y_p)/\Delta y_j$, $f_y^- = 1 - f_y^+$, $f_z^+ = (z_{k+1} - z_p)/\Delta z_k$, $f_z^- = 1 - f_z^+$, and $\Delta x_i = x_{i+1} - x_i$, $\Delta y_j = y_{j+1} - y_j$ and $\Delta z_k = z_{k+1} - z_k$. Contrastingly, a particle of rest mass m_a at $\boldsymbol{r}_p$ contributes to E, J_l and S_{lm} of the nearest 8 grid points as

$$
\begin{aligned}
E&_{i+1/2\mp1/2,\ j+1/2\mp1/2,\ k+1/2\mp1/2} \\
&= \frac{f_x^\pm f_y^\pm f_z^\pm}{\Delta V_{ijk}} m_a u_a^0 (\alpha e^{-6\phi})_{i+1/2\mp1/2,\ j+1/2\mp1/2,\ k+1/2\mp1/2},
\end{aligned} \tag{6·7}
$$

$$
\begin{aligned}
(J_l)&_{i+1/2\mp1/2,\ j+1/2\mp1/2,\ k+1/2\mp1/2} \\
&= \frac{f_x^\pm f_y^\pm f_z^\pm}{\Delta V_{ijk}} m_a (u_l)_a (e^{-6\phi})_{i+1/2\mp1/2,\ j+1/2\mp1/2,\ k+1/2\mp1/2},
\end{aligned} \tag{6·8}
$$

$$
\begin{aligned}
(S_{lm})&_{i+1/2\mp1/2,\ j+1/2\mp1/2,\ k+1/2\mp1/2} \\
&= \frac{f_x^\pm f_y^\pm f_z^\pm}{\Delta V_{ijk}} m_a \left(\frac{u_l u_m}{u^0}\right)_a \left(\frac{1}{\alpha e^{6\phi}}\right)_{i+1/2\mp1/2,\ j+1/2\mp1/2,\ k+1/2\mp1/2},
\end{aligned} \tag{6·9}
$$

where $\Delta V_{ijk} = \Delta x_i \Delta y_j \Delta z_k$. These matter densities are computed by summing up the contributions of all the nearby particles. We note that in the CIC scheme, second order accuracy in Δx_i, Δy_j and Δz_k is preserved.

In solving equations of motion for particles, we use the second order Runge-Kutta method, accurate to $O(\Delta t^2)$. [18] As in the case of computation of evolution equations for geometric variables, we use appropriate extrapolation and interpolation to maintain second order accuracy in time. Hence the CIC scheme we use here is second order accurate in time and space.

6.3. *Grid, time step, logical flow, grid and particle numbers*

Throughout this paper, we use a fixed uniform grid, i.e., $\Delta x_0 = \Delta x_1 = \cdots = \Delta x_i = \cdots \equiv \Delta x$ and $\Delta x = \Delta y = \Delta z =$const. We also take an equal number of grid points in each direction.

Time step Δt must satisfy the stability condition imposed by the Courant criterion for geometric variables. In the case of a zero shift vector, the geometric Courant condition is written as

$$\Delta t < \alpha^{-1} \times \min(\sqrt{\gamma_{xx}}\Delta x, \sqrt{\gamma_{yy}}\Delta y, \sqrt{\gamma_{zz}}\Delta z). \tag{6.10}$$

Since the relation $\alpha^{-1}\sqrt{\gamma_{ii}} > 1$ holds for most problems considered in this paper, we simply set a geometric time step which satisfies the geometric Courant condition as

$$\Delta t_g = C_g \Delta x, \tag{6.11}$$

where C_g is a constant which we choose as 0.1 or 0.2. Also, Δt must be sufficiently small so that the matter distribution cannot change by a large fraction. The time scale is shortest when the matter distribution changes in a dynamical manner such as in the case that the matter collapses to a singularity. Taking into account the above constraints, we simply set

$$\Delta t = \min\left(C_m \sqrt{\frac{3\pi}{32Ee^{6\phi}}}, \Delta t_g \right), \tag{6.12}$$

where C_m is a constant which we choose as $C_m = 0.01$. Note that the first term on the right-hand side of Eq. (6.12) denotes the time for the collapse to a singularity of a spherical, homogeneous dust in the Newtonian limit.

The logical flow in the numerical simulation is as follows:
1. Set an initial condition and start the simulation.
2. Choose the time step Δt.
3. $\tilde{A}_{ij}$, K, $\tilde{\gamma}_{ij}$, ϕ and F_i evolve.
4. Impose boundary conditions for $\tilde{A}_{ij}$, K, $\tilde{\gamma}_{ij}$, ϕ and F_i.
5. Determine α using an approximate maximal slice condition.
6. Search for the apparent horizon (every ~ 10 time steps).
7. Calculate the force terms in the equations of motion for particles by means of the CIC interpolation.
8. Solve the equations of motion for the particles.
9. Assign E, J_i and S_{ij} at each grid point using the CIC assignment method.
10. Return to step 2, and repeat the steps 2–9.

Note that when we adopt a spatial gauge condition, we solve an equation for β^k between steps 5 and 6.

In the simulations whose results are reported below besides test-bed simulations performed in §7, we take 101^3 grid points covering a single octant of $0 \leq x, y, z \leq L$, where we set L typically as $15M$. All the rest masses of particles m_a are chosen to be identical with m, which is adjusted to satisfy $M = 1$ initially (i.e., $M_* = 8Nm > M = 1$). The particle number is set to $N = 10^5$. For one simulation, it required typically about 16 CPU hours for about 3000 time steps using one of four CPUs of the FACOM VX/4R machine in the data processing center of NAOJ.

§7.   Test-bed computations

Before we give the main numerical results, we demonstrate that our numerical code can generate exact (or nearly exact) solutions accurately.

7.1. *Newtonian collapse*

First, following Shapiro and Teukolsky,[19)] we show that our CIC code for particles accurately computes Newtonian gravitational collapse. For Newtonian simulations, we use the equations

$$\frac{dx^i}{dt} = v^i, \tag{7·1}$$

$$\frac{dv^i}{dt} = U_{,i}, \tag{7·2}$$

$$\Delta U = -4\pi\rho, \tag{7·3}$$

where the first two equations constitute equations of motion for particles, and the last one is the Poisson equation for the Newtonian potential U. (The Poisson equation for U is solved with our Poisson solver used in solving ψ and α in the initial value problem (§5).) Using the CIC scheme, we interpolate U at each particle position, and assign ρ at each grid point.

As benchmark simulations, we use gravitational collapses of homogeneous, axially symmetric or triaxial ellipsoids of axial length a_1, a_2 and a_3, because we can obtain solutions for such cases easily by solving the following ordinary differential equations for the axial length:

$$\frac{d^2a_1}{dt^2} = -\frac{3MA_1}{2a_2a_3}, \tag{7·4}$$

$$\frac{d^2a_2}{dt^2} = -\frac{3MA_2}{2a_1a_3}, \tag{7·5}$$

$$\frac{d^2a_3}{dt^2} = -\frac{3MA_3}{2a_1a_2}. \tag{7·6}$$

Here we do not take into account the rotational motion of particles. (Note that for ρ =constant, the Newtonian potential is $U = \pi\rho \sum_{k=1}^{3} A_k(a_k^2 - x_k^2)$ and $(x_1, x_2, x_3) = (x, y, z)$.[20)]) In the benchmark simulations, we use a 61^3 grid covering a single octant. In Figs. 1(a) and (b), we give results for two cases as examples. In each figure, we plot the mean axial length, defined as

$$\sqrt{\langle x_i^2 \rangle} \equiv \left(\frac{1}{N} \sum_{i=1}^{N} x_i^2\right)^{1/2}, \tag{7·7}$$

and the total energy of the system as functions of time. The solid lines and filled circles denote (nearly) exact and numerical solutions, respectively. In Fig. 1(a), we give results for an axially symmetric prolate collapse with initial axial length $a_3 = 3M$ and $a_1 = a_2 = 2.4M$, while in Fig. 1(b), results for the collapse of a
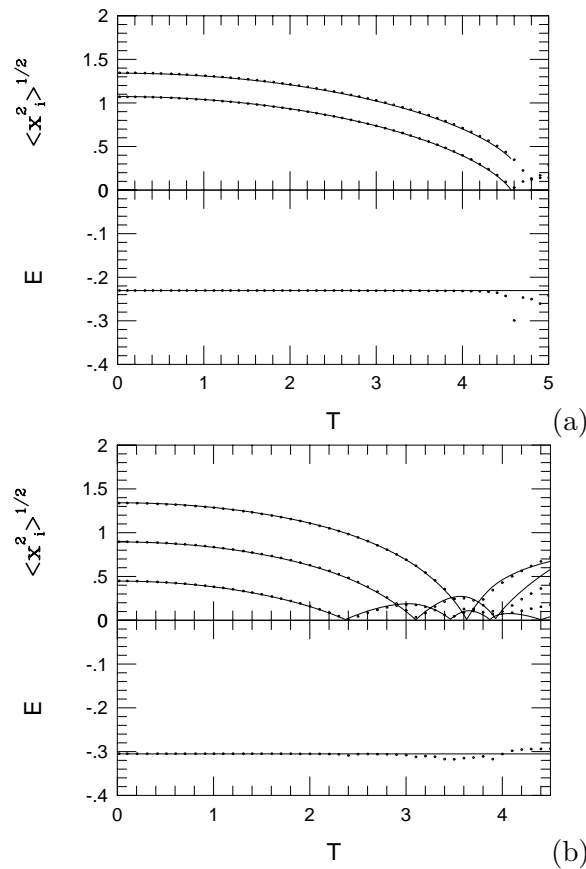
Fig. 1. The mean square axial length and the energy as functions of time in Newtonian homogeneous dust collapse: (a) prolate spheroid collapse with initial axial length $a_3 = 3M$ and $a_1 = a_2 = 2.4M$; (b) ellipsoid collapse with initial axial length $a_1 = 3M$, $a_2 = 2M$ and $a_3 = M$. The solid lines and filled circles denote (nearly) exact and numerical solutions, respectively. T and E are shown in units of M.

triaxial ellipsoid with initial axial length $a_1 = 3M$, $a_2 = 2M$, and $a_3 = M$ are shown. It is found that in each case, numerical results agree with (nearly) exact solutions fairly accurately, except for the case in which the axial length of one of the axes becomes very small and numerical resolution is insufficient. We note that in the case of the prolate collapse, the length of the minor axes becomes zero at $t \simeq 4.6M$, and a singularity is formed. If the system maintains strict axial symmetry, the simulation will be terminated, but in this 3D simulation, axial symmetry is slightly broken, and the simulation proceeds. However, for $t > 4.6M$, the accuracy of the energy conservation is too poor, and hence, numerical results are not reliable. This implies that even when a simulation can continue after the collapse of the minor axes, we should terminate it if the resolution becomes insufficient.

7.2. *Stability of general relativistic spherical equilibrium dust balls*

A first test of our general relativistic code is provided by the case of a spherical dust ball whose particles all move in circular orbits at $t = 0$.[21] The orbits are

assumed to be isotropically distributed in the transverse direction perpendicular to the radial vector. The dust ball is initially in equilibrium, and if stable, the configuration should be kept (nearly) static for a long time in numerical computation.

The equilibrium dust ball is obtained as follows. We choose the line element in the isotropic coordinate form as

$$ds^2 = -\alpha^2 dt^2 + \psi^4(dr^2 + r^2 d\theta^2 + r^2 \sin^2\theta d\varphi^2). \tag{7·8}$$

Since each particle is in a circular orbit at each radius, we can derive $L(r)^2 \equiv u_i u^i = (u_\theta^2 + u_\varphi^2/\sin^2\theta)r^{-2}\psi^{-4}$ from the geodesic equation as

$$L(r)^2 = \frac{\partial_r \alpha}{\alpha}\left(\frac{2\partial_r \psi}{\psi} - \frac{\partial_r \alpha}{\alpha} + \frac{1}{r}\right)^{-1}. \tag{7·9}$$

Using $L(r)$, equations for ψ and α are written as

$$\left(\partial_r^2 + \frac{2}{r}\partial_r\right)\psi = -2\pi\rho_*\sqrt{1 + L(r)^2}\psi^{-1}, \tag{7·10}$$

$$\left(\partial_r^2 + \frac{2}{r}\partial_r\right)(\alpha\psi) = 2\pi\rho_*\alpha\psi^{-1}\frac{1 + 3L(r)^2}{\sqrt{1 + L(r)^2}}. \tag{7·11}$$

Hence, if we give an arbitrary configuration of $\rho_*(r)$, the corresponding equilibrium state for the dust ball is obtained by solving Eqs. (7·10) and (7·11) iteratively. In this test, we set ρ_* as Eq. (5·8).

Stability of a dust ball in equilibrium is simply found if we consider the stability of each particle. [21] Orbits of particles at r are stable if the condition

$$M(r) < \frac{1}{6}r\psi(r)^2 \tag{7·12}$$

is satisfied. Otherwise, they are unstable. Here, $M(r)$ denotes the gravitational mass inside r, i.e.,

$$M(r) = 4\pi \int_0^r \rho_*\psi^{-1}\sqrt{1 + L(r')^2}r'^2 dr'. \tag{7·13}$$

If all the particles satisfy the condition (7·12), the dust ball is stable. From numerical computations, we have found that for $r_o < 5.28M_*$ (or $r_o < 5.53M$), the dust ball is unstable, and otherwise it is stable.

We performed 3D simulations using the above spherical equilibrium dust ball as initial conditions. We note that in these simulations, we change outer boundary conditions of geometric variables as

$$h_{ij} = \tilde{A}_{ij} = F_i = 0, \tag{7·14}$$

because the spacetime is spherically symmetric and almost static. In this subsection, we set $M_* = 1$ (i.e., $m = 1/N$), and the time and length are given in units of M_*. The simulation was performed using 51^3 and 76^3 uniform grids with $\Delta x = r_o/20$ and $\Delta x = r_o/30$, respectively. We chose $N = 5 \times 10^4$ in this test.

In Fig. 2, we display the time evolution of the mean axial length of the x-component defined in Eq. (7·7) for a stable equilibrium dust ball of $r_o = 6M_*$ and an unstable equilibrium dust ball of $r_o = 5M_*$. Note that for $r_o = 6M_*$ and $r_o = 5M_*$, $M = 0.957M_*$ and $0.954M_*$, respectively. For $r_o = 6M_*$, the orbital period P of a particle at $r = 6M_*$ is about $118M_*$, and for $r < 6M_*$, P is smaller. For $r_o = 5M_*$, $P = 95M_*$ for a particle at $r = 5M_*$. In addition to equilibrium dust balls, we also adopt non-equilibrium ones in which we initially reduce $L(r)$ by 1% for all the particles.

The solid and dashed lines denote the results for equilibrium and non-equilibrium dust balls with 76^3 grid. The dotted line denotes the result for the equilibrium dust ball of $r_o = 6M_*$ with 51^3 grid. From Fig. 2, it is clearly seen that the equilibrium dust ball of $r_o = 6M_*$ is kept stable for a long time. We note that the dust ball is not static,
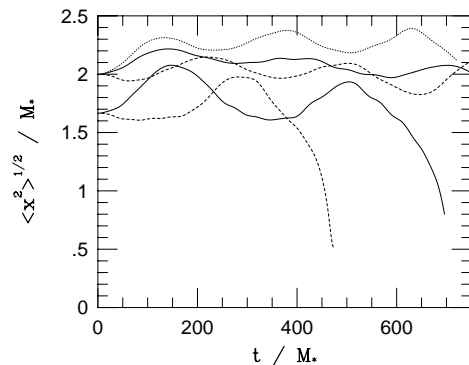

Fig. 2. The mean square axial length of the x-axis as a function of time for equilibrium dust balls. The solid and dashed lines, respectively, denote the results for a 76^3 grid with equilibrium dust balls and for non-equilibrium dust balls for which the angular momentum of all particles is slightly reduced initially. The dotted line denotes the result for a 51^3 grid with an equilibrium dust ball of $r_o = 6M_*$. For $r_o = 6M_*$, the initial value of $\langle x^2 \rangle^{1/2} \simeq 2M_*$, and for $r_o = 5M_*$ it is $\simeq 1.67$. We note that results for y and z-components are the same as those for x-components.

but oscillates after an initial expansion. This expansion and oscillation are due mainly to a slight inconsistency between the initial data, which is produced by 1D code, and the 3D evolution scheme. This is a purely numerical effect. In reality, the oscillation amplitude decreases with improved resolution (compare results of 76^3 and 51^3 simulations for the equilibrium dust balls of $r_o = 6M_*$). We confirm the stability of the dust ball of $r_o = 6M_*$ again by finding the stable oscillation of the angular momentum depleted, non-equilibrium ball.

On the other hand, for the case of $r_o = 5M_*$, the dust balls are unstable irrespective of the initial perturbation. We note again that the initial expansion seen in Fig. 2 is due to a slight inconsistency between the initial data and the 3D evolution scheme. Although the dust balls initially expand, they eventually collapse to become BHs because the angular momenta of the particles are not sufficient to overcome the self-gravity. Thus, we may conclude that the equilibrium dust ball of $r_o = 5M_*$ is unstable against gravitational collapse and that our numerical code can judge the stability of the dust balls.

7.3. *General relativistic spherical collapse and Teukolsky waves*

As second and third tests of our general relativistic code, we make use of two dynamical solutions. One is a solution of a spherical symmetric dust collapse, and the other is the Teukolsky linear gravitational wave.[9), 15), 6)]

In spherical dust collapse, we use the initial configuration

$$\rho_* = f(s) = \begin{cases} \rho_0 \left[1 + e^{(s^{2/3}-1)/\epsilon} + \dfrac{2s^{2/3}}{3\epsilon} e^{(s^{2/3}-1)/\epsilon} \right]^{-1}, & 0 \le s \le 1, \\ 0, & s > 1, \end{cases} \qquad (7\cdot15)$$

where ϵ is a small parameter ($\ll 1$), s is related to the isotropic radial coordinate as

$$r = r_0 [s(1 + e^{(s^{2/3}-1)/\epsilon})]^{1/3}, \qquad (7\cdot16)$$

and r_0 is an approximate coordinate radius of the initial configuration. Here, ρ_0 is adjusted to set the gravitational mass to $M = 1$. Since ϵ is small, ρ_* is almost constant, except for the region $r \sim r_0$ (see Fig. 3 for $\epsilon = 0.08M$). In particular, ρ_* becomes constant in the limit $\epsilon \to 0$. To prepare (nearly) exact solutions of the dust collapse, we perform spherically symmetric simulations using our 1D code, which has been already confirmed to generate accurate results by comparison with an exact solution (Oppenheimer-Snyder solution). [22)]
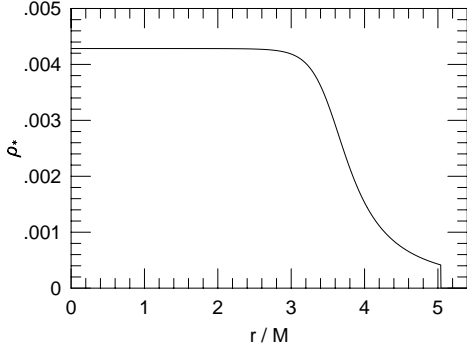
Fig. 3. Initial profile of ρ_* as a function of r for a relativistic spherical dust collapse ($\epsilon = 0.08M$).

In Figs. 4(a) and (b), we show α at $r = 0$ as a function of time and α along the x-axis at $t = 12.0M$, $20.1M$ and $23.5M$, respectively. The simulation was performed for $r_0 = 4M$ and $\epsilon = 0.08M$ with 61^3 grid numbers covering a region $0 \le x,\ y,\ z \le 9M$. ($M_* \simeq 1.143M$ in this case.) The solid and dotted lines show results obtained using 3D and 1D codes, respectively. Note that at $t \sim 20.7M$, an apparent horizon was formed in this solution, and our 3D apparent horizon finder correctly finds it. (In Fig. 5, we plot snapshots of
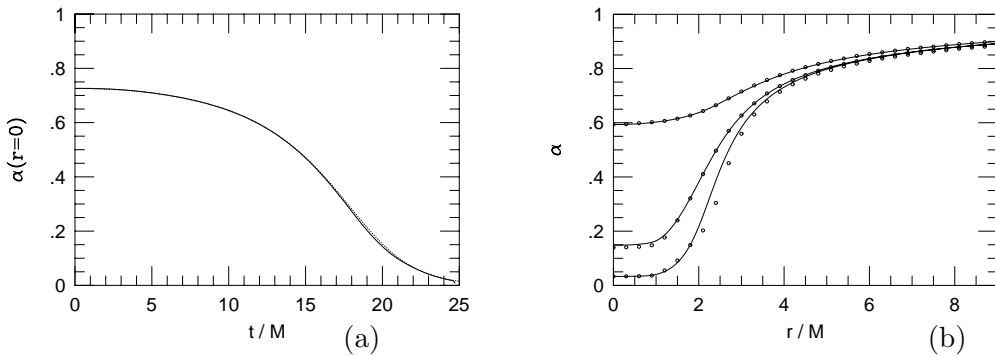

Fig. 4. (a) α at $r = 0$ as a function of t for spherical dust collapse. The solid and dotted lines correspond to 3D and 1D results, respectively. (b) α as a function of r at selected times ($t = 12.0M, 20.1M$, and $23.5M$). The solid and open circles are 3D and 1D results, respectively.

the particle positions and location of the apparent horizon at $t = 21.8M$). Note also that the 3D simulation halts at $t \sim 25M$ because the gradient of the geometric variables near the apparent horizon is too steep. Figure 4 demonstrates that our 3D code can generate a fairly accurate result up to $t \sim 24M$ when the apparent horizon was already formed. We emphasize that in the 1D simulation, we use the maximal slice condition, while in the 3D simulation, we use an "approximate" such condition. Nevertheless, the two results agree fairly well. This suggests that the approximate maximal slice condition is actually a good approximation of the maximal slice condition, at least up to the formation of BHs, and hence, the slice is expected to have a singularity avoidance property.

We also investigate whether our 3D code can compute a solution of the Teukolsky wave accurately. In a previous paper,[6] we performed the same test using maximal, harmonic, and geodesic slice conditions. However, throughout this paper, we perform the simulation in an "approximate" maximal slice, so that re-examination is necessary. As the initial conditions of the Teukolsky wave, we set a conformal flat and time-asymmetric initial data, as adopted in our previous paper.[6] For the initial condition, components of $\hat{A}_{ij}$ are given by

$$\hat{A}_{xx} = \frac{A}{12} \exp\left(-\frac{r^2}{2}\right)[12 - 8y^2 - 16z^2 + 2z^4 + z^2(x^2 + 3y^2) + y^4 - x^2y^2], \quad (7 \cdot 17)$$

$$\hat{A}_{yy} = \frac{A}{12} \exp\left(-\frac{r^2}{2}\right)[-12 + 8x^2 + 16z^2 - 2z^4 - z^2(3x^2 + y^2) - x^4 + x^2y^2], (7 \cdot 18)$$

$$\hat{A}_{zz} = \frac{A}{12} \exp\left(-\frac{r^2}{2}\right)(x^2 - y^2)(-8 + 2z^2 + x^2 + y^2), \quad (7 \cdot 19)$$

$$\hat{A}_{xy} = \frac{A}{12} \exp\left(-\frac{r^2}{2}\right)(x^2 - y^2)xy, \quad (7 \cdot 20)$$
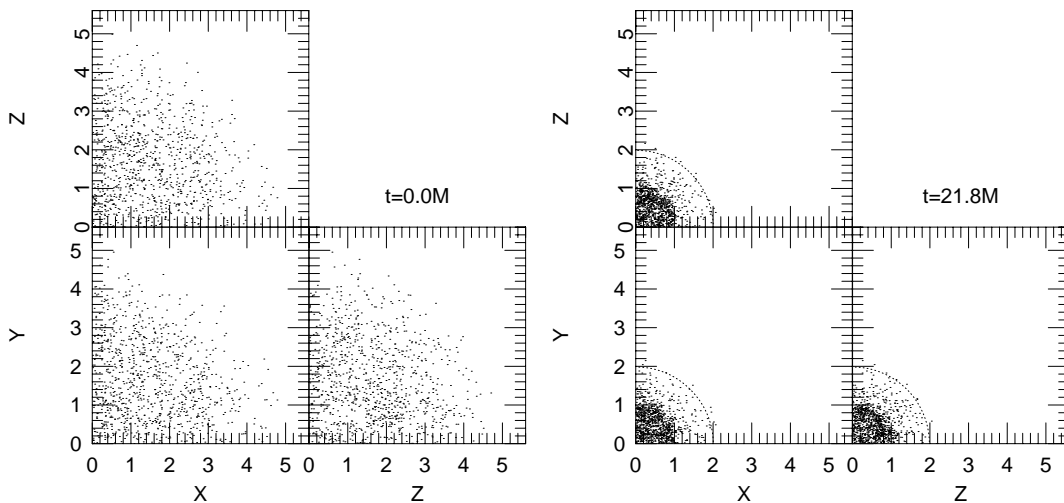

Fig. 5. Snapshots of the particle positions (dots) and location of the apparent horizon (dotted lines) at $t = 0$ and $21.8M$ for spherical dust collapse. Only 10^3 out of 10^5 particles are plotted. The positions are shown in units of M and are projected onto x-y, y-z and z-x planes.

$$\hat{A}_{xz} = \frac{A}{12} \exp\left(-\frac{r^2}{2}\right)(12 - 2r^2 + x^2 - y^2)xz, \tag{7.21}$$

$$\hat{A}_{yz} = \frac{A}{12} \exp\left(-\frac{r^2}{2}\right)(-12 + 2r^2 + x^2 - y^2)yz. \tag{7.22}$$
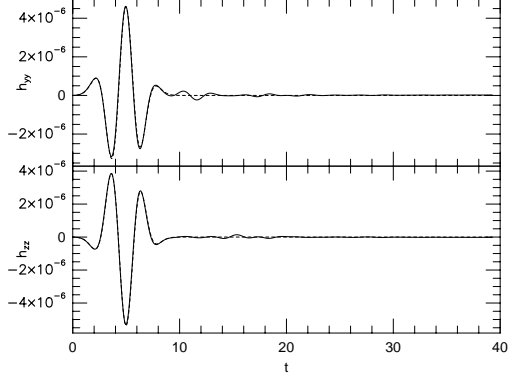

Fig. 6. h_{yy} and h_{zz} at $(x, y, z) = (4.9, 0, 0)$ as a function of t for a low amplitude Teukolsky wave. We adopt the width of the wave packet of gravitational waves as the length and time units. The solid and dashed lines denote the numerical and exact solutions, respectively.

Following a previous paper,[6] we adopt the width of the wave packet of gravitational waves as the time and length units.

In Fig. 6, we show h_{yy} and h_{zz} at $(4.9, 0, 0)$. Here, the coordinate radius at the outer boundary along the x-axis is set to be 5. As the amplitude of gravitational waves at $t = 0$, we choose $A = 10^{-4}$. We use 51^3 for the grid size in this simulation. The solid and dashed lines denote the numerical and analytic solutions, and they show that our code accurately computes a Teukolsky wave.

In this simulation, we continue the computation after the wave packet passes through outer boundaries in order to check whether the simulation can be stably carried out for a sufficiently

Table I. The list of initial conditions for simulations in §8, and the final fates. M denotes the total mass of the system.

(a) Triaxial collapses.

Shape	Axial length (c_x, c_y, c_z)	Rest mass M_*	Final fate	Figure
Oblate	$(4M, 4M, 2M)$	$1.172M$	Black hole	Fig. 7
Prolate	$(4M, 2M, 2M)$	$1.216M$	Black hole	Fig. 8
Prolate	$(4M, M, M)$	$1.300M$	Spindle	Fig. 9
Triaxial	$(4M, 2M, M)$	$1.251M$	Black hole	Fig. 10

(b) Spheroidal collapses of co-rotating and counter-rotating particles of $r_0 = 4M$.

Ω at $t = 0$	Rest mass M_*	Final fate	Figure
$1.2\sqrt{M/r_0^3}$	$1.061M$	Black hole	Fig. 11
$1.4\sqrt{M/r_0^3}$	$1.036M$	Ring	Fig. 12

(c) Head-on collisions of two spherical clusters. ($r_6 = r_o/6$ and $M = 2M_{one}$.)

M_{one}/r_6	Total rest mass M_*	Boost velocity a	Final fate	Figure
1	$1.088M$	$0.1r_6$	Black hole	Fig. 13
1	$1.015M$	$0.3r_6$	Black hole	Fig. 14
0.5	$1.043M$	$0.1r_6$	Black hole	Fig. 15
0.3	$1.024M$	$0.1r_6$	Black hole	Fig. 15
0.25	$1.020M$	$0.1r_6$	New equilibrium	Figs. 15, 16

long time at least for a weakly curved, dynamical spacetime. This test should be performed, because the simulation cannot be continued if we fail to select an appropriate gauge condition [6] or an appropriate formalism, [23] and by this test, we can clarify this point. Figure 6 apparently indicates that our code passes this examination.

§8. Numerical results on formation of black holes

In this section, we give results for a wide variety of numerical simulations. In Table I, we list the initial conditions and final products in the simulations.
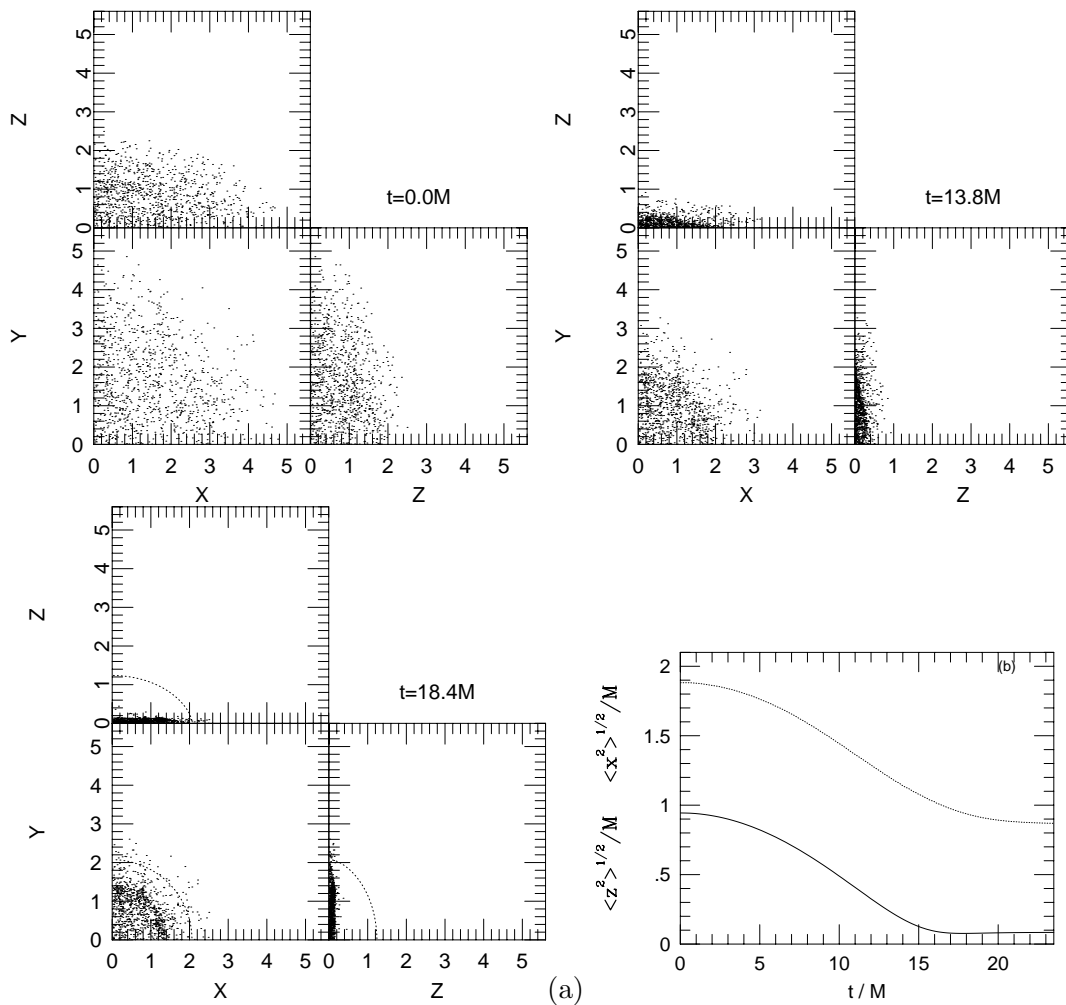
Fig. 7. Snapshots of the particle positions (dots) and location of the apparent horizon (dotted lines) at selected times for oblate dust collapse. Only 10^3 out of 10^5 particles are plotted. The positions are shown in units of M and are projected onto x-y, y-z and z-x planes. Figure (b) displays the time evolution of the mean axial length of x-axis (dotted line) and z-axis (solid line).

8.1. *Triaxial collapses from time-symmetric initial conditions*

To give the initial density profile, we set ρ_* which we chose in §7 as

$$\rho_* = f(s). \tag{8.1}$$

Here, however, for setting non-axisymmetric profiles, s is related to spatial coordinates as

$$\left(\frac{x^2}{c_x^2} + \frac{y^2}{c_y^2} + \frac{z^2}{c_z^2}\right)^{3/2} = s(1 + e^{(s^{2/3}-1)/\epsilon}), \tag{8.2}$$

where c_x, c_y and c_z denote the characteristic coordinate length of ellipsoids. ρ_0 is adjusted so that $M = 1$ again. For obtaining the initial condition of geometric variables, we need to solve only the Hamiltonian constraint with $E = \rho_* \psi^{-6}$.
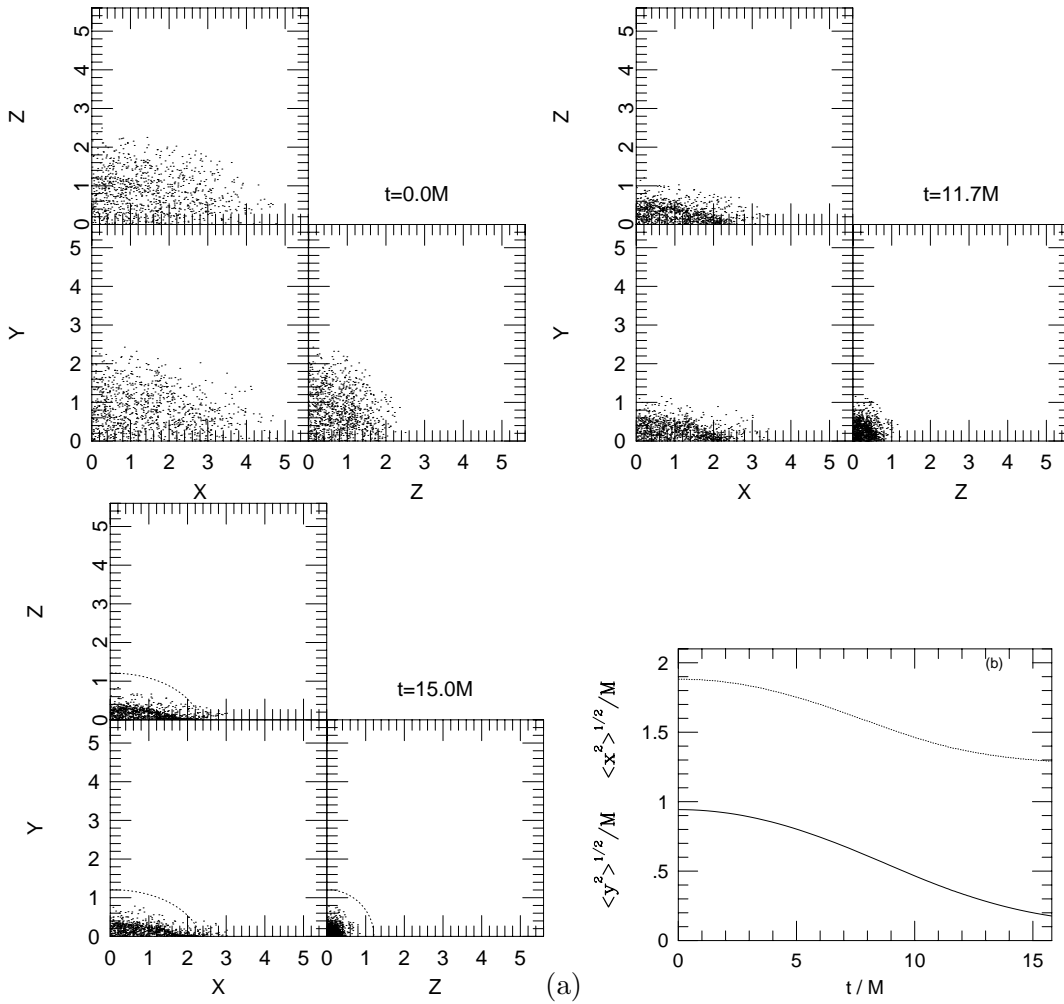
Fig. 8. The same as Fig. 7, but for prolate collapse of the initial axial length of minor and major axes $2M$ and $4M$, respectively. (The x-axis is the major axis.) Figure (b) exhibits the time evolution of mean axial length of x-axis (dotted line) and y-axis (solid line).

We perform numerical simulations for four cases changing (c_x, c_y, c_z): (1) an oblate collapse, $(4M, 4M, 2M)$; (2) prolate collapses, $(4M, 2M, 2M)$ and $(4M, M, M)$; (3) a triaxial collapse, $(4M, 2M, M)$. In each case, M_* is about 1.172, 1.216, 1.300 and $1.251M$, respectively. In Figs. 7–10, we display snapshots of the particle positions at selected times. The particle positions are plotted in units of M, and are projected onto x-y, y-z and z-x planes.

For the case of oblate collapse, the minor axis collapses first, and as a result, a disk-like object is formed. The density in the disk is very high, but the disk has a finite thickness (Fig. 7(b)) because the collapse is not completely coherent. As a result, the geodesic equations and equations for geometric variables can be integrated without any special technique,[24] and the simulation is continued. (Even when the collapse is coherent and the thickness of the disk is zero, the simulation can be continued in principle because in the disk, the geodesic equations can be
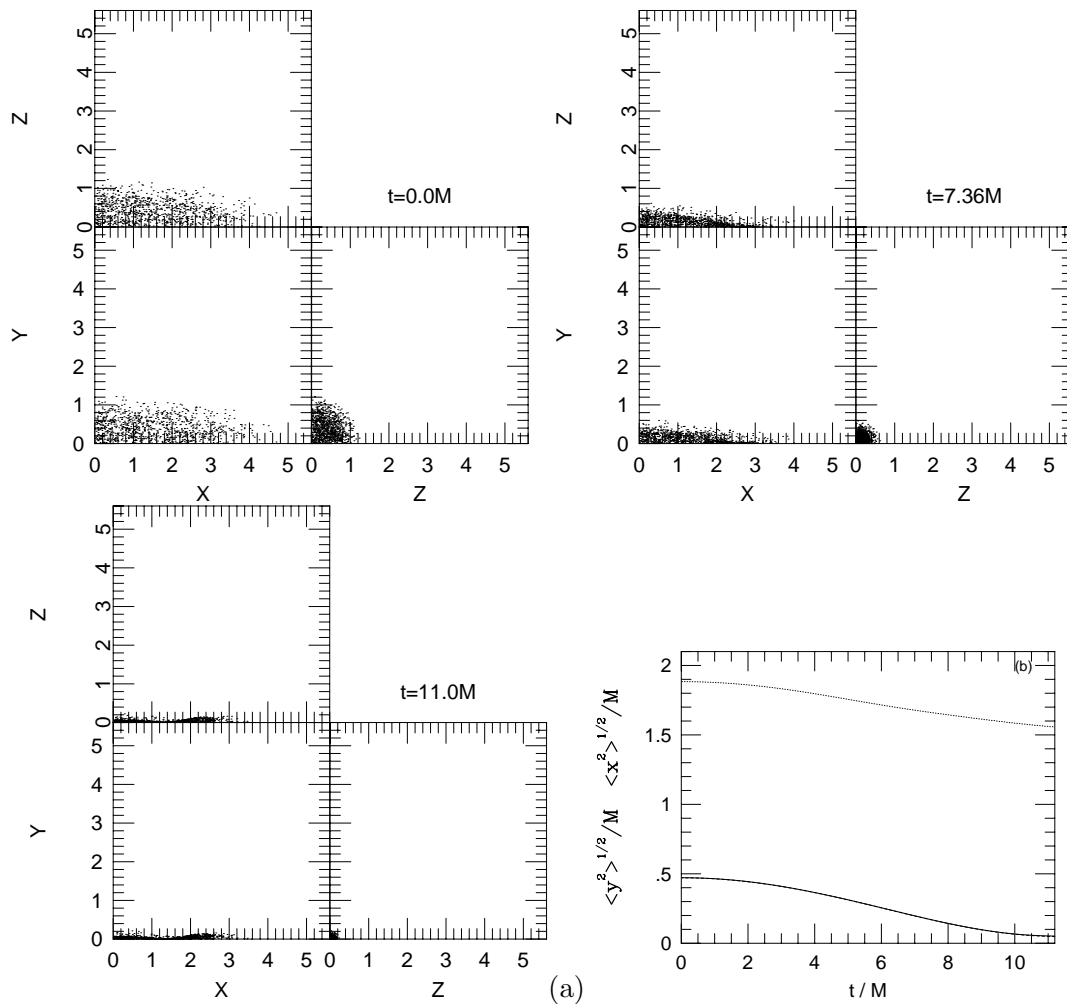

Fig. 9. The same as Fig. 8, but for prolate collapse of initial mean axial length of minor and major axes M and $4M$, respectively.

integrated. [24]) After the formation of the disk, its radius shrinks gradually due to self-gravity, and finally a BH is formed.

For the case of prolate collapses, the two minor axes collapse first, and thus a spindle-like object is formed. In contrast to the above oblate case, the thickness of the spindle gradually approaches zero (Figs. 8(b) and 9(b)), because the self-gravity is stronger than that for the case of the oblate collapse. Hence, if an event horizon is not formed, the object will ultimately be a naked singularity. [25]) For the case in which the initial axial ratio of the major axis to that of the minor axis is not large, the major axis also collapses quickly. Then, before a spindle singularity is formed, an apparent horizon (i.e., BH) is formed. On the other hand, when the initial axial ratio is large, we could not find the apparent horizon before the simulation is halted due to the formation of a spindle-like singular object along the z-axis. Such a feature is essentially the same as that found previously by Shapiro and Teukolsky. [25]) Thus, the
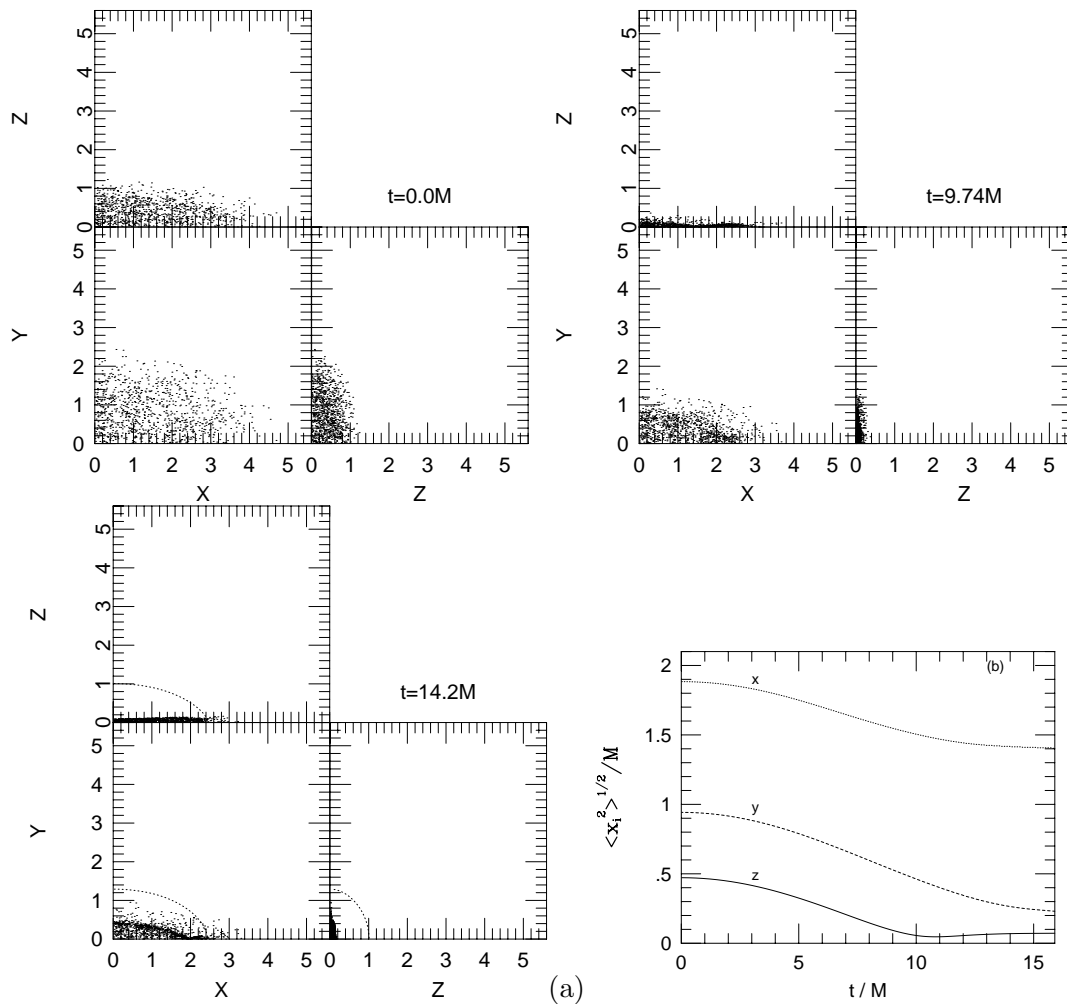

Fig. 10. The same as Fig. 7, but for collapse of a triaxial ellipsoid of initial mean axial length $4M, 2M$ and M.

simulation may suggest that (if the axial symmetry is always maintained) a naked singularity is formed, although we cannot draw any strong conclusion because an event horizon may be formed.[26]

For the case of triaxial collapse, the features of the evolution are similar to those of oblate collapse rather than prolate collapse. First, the shortest axis collapses, and an ellipsoidal disk-like object is formed. In this case, also, the thickness of the disk is finite (Fig. 10(b)). After the formation of the disk, the second longest and longest axes subsequently collapse, and finally a BH is formed. In contrast to the above prolate collapses, the mean axial length of the shortest axis never approaches zero, but bounces at a minimum thickness. This seems to be because in the triaxial collapses, the mean axial lengths of the two minor axes are not equal, and the self-gravity is not as strong as that in the case of prolate collapse. Hence, we guess that
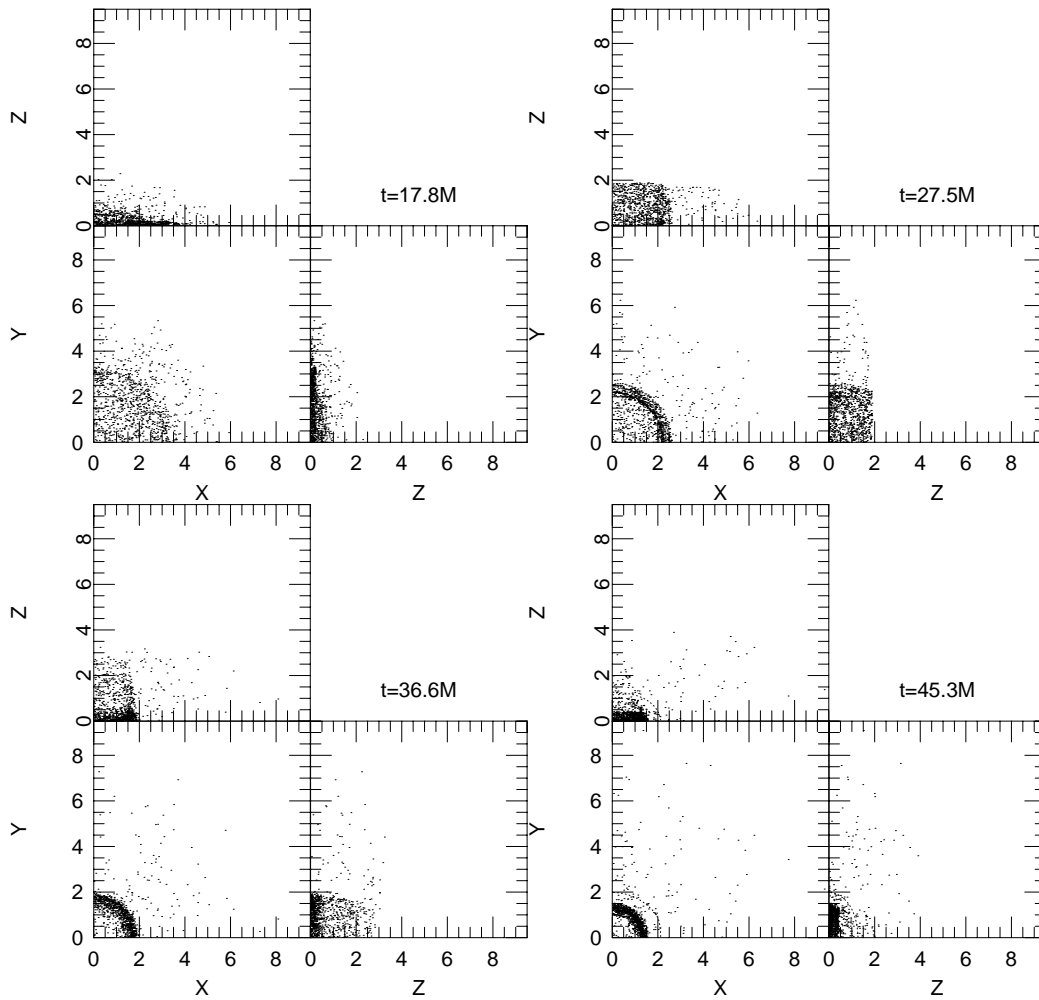

Fig. 11. The same as Fig. 7, but for collapse of co-rotating and counter-rotating particles with $\Omega = 1.2(M/r_0^3)^{1/2}$ and $r_0 = 4M$. Note that at $t = 0$, the particle positions are the same as those exhibited in Fig. 5.

a singularity will not be formed in triaxial collapses.

8.2. *Collapses of spheroids of co-rotating and counter-rotating particles*

In this subsection, we give numerical results on the collapse of spheroids composed of co-rotating and counter-rotating particles setting initial conditions in which the matter consists of equal numbers of co-rotating and counter-rotating particles. For each pair of particles, the initial four-velocity components are set as

$$(u_x, u_y, u_z) = (\mp \Omega \psi^2 y, \pm \Omega \psi^2 x, 0). \tag{8.3}$$

As in a previous section, we set $\rho_* = f(s)$ with $r = r_0[s(1+e^{(s^{2/3}-1)/\epsilon})]^{1/3}$ (Eq. (7·16)), where we choose $r_0 = 4M$ and $\epsilon = 0.08$.

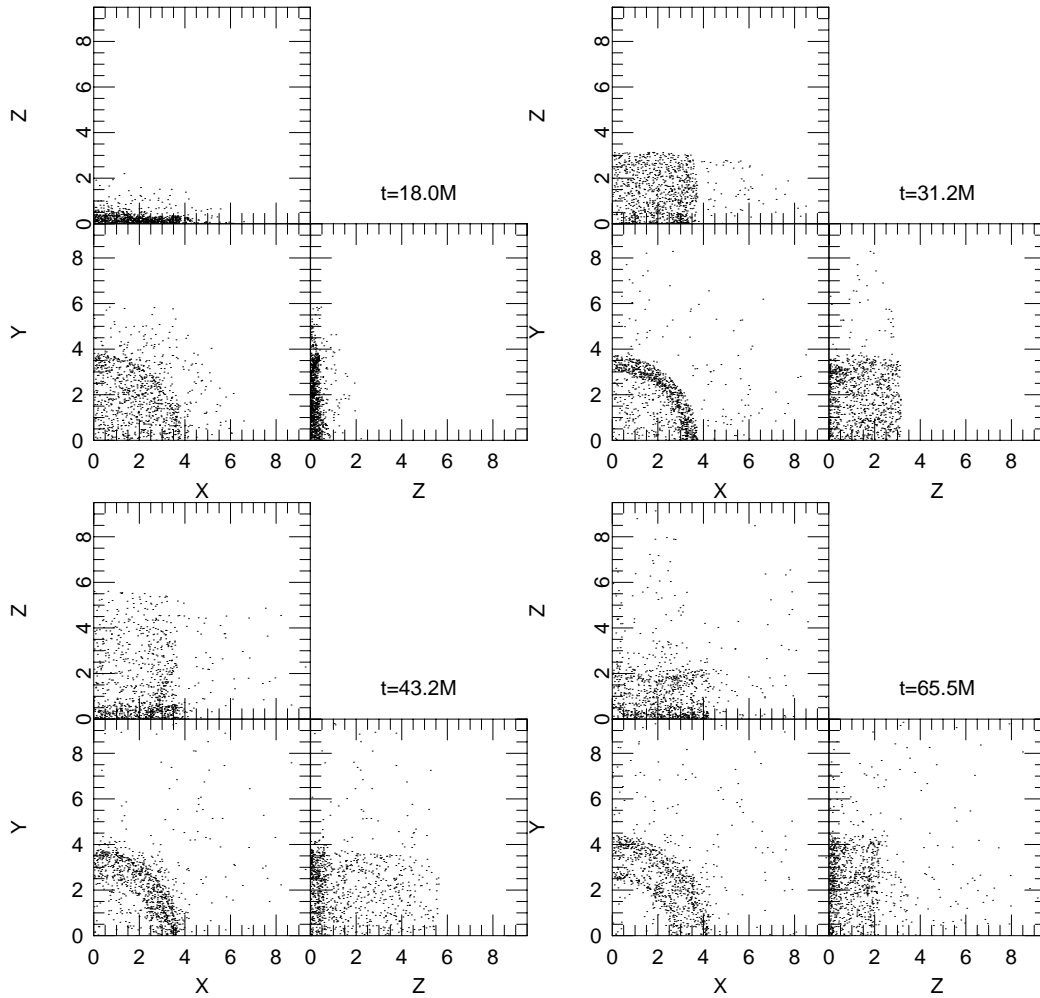Since $J_i = 0$, the initial slice is time-symmetric (i.e., $K = \tilde{A}_{ij} = 0$), so that we

Fig. 12. The same as Fig. 7, but for collapse of co-rotating and counter-rotating particles with $\Omega = 1.4(M/r_0^3)^{1/2}$ and $r_0 = 4M$. Note that the particle positions at $t = 0$ are the same as those in Fig. 5.

only need to solve the Hamiltonian constraint equation, which is essentially the same as that in the case of $u_i = 0$, except for the fact $\alpha u^0 \neq 1$, which slightly changes the initial form of E to

$$E = \rho_* \psi^{-6} \sqrt{1 + \Omega^2 (x^2 + y^2)}. \tag{8.4}$$

In Figs. 11 and 12, we show snapshots of the particle positions at selected times for $\Omega = 1.2\sqrt{M/r_0^3}$ ($M_* \simeq 1.061M$) and $\Omega = 1.4\sqrt{M/r_0^3}$ ($M_* \simeq 1.036M$), respectively. In both cases, for early times, gravitational collapse proceeds only in the z-direction, and the other two axes do not change much due to the centrifugal force. As a result, a disk-like object is formed. Since the collapse is not coherent, the thickness of the disk again remains finite. After the formation of the disk, particles around $r = 0$ move outward because of the centrifugal force, while those at large radii move inward due to gravity. As a result, a ring is formed. If the initial value
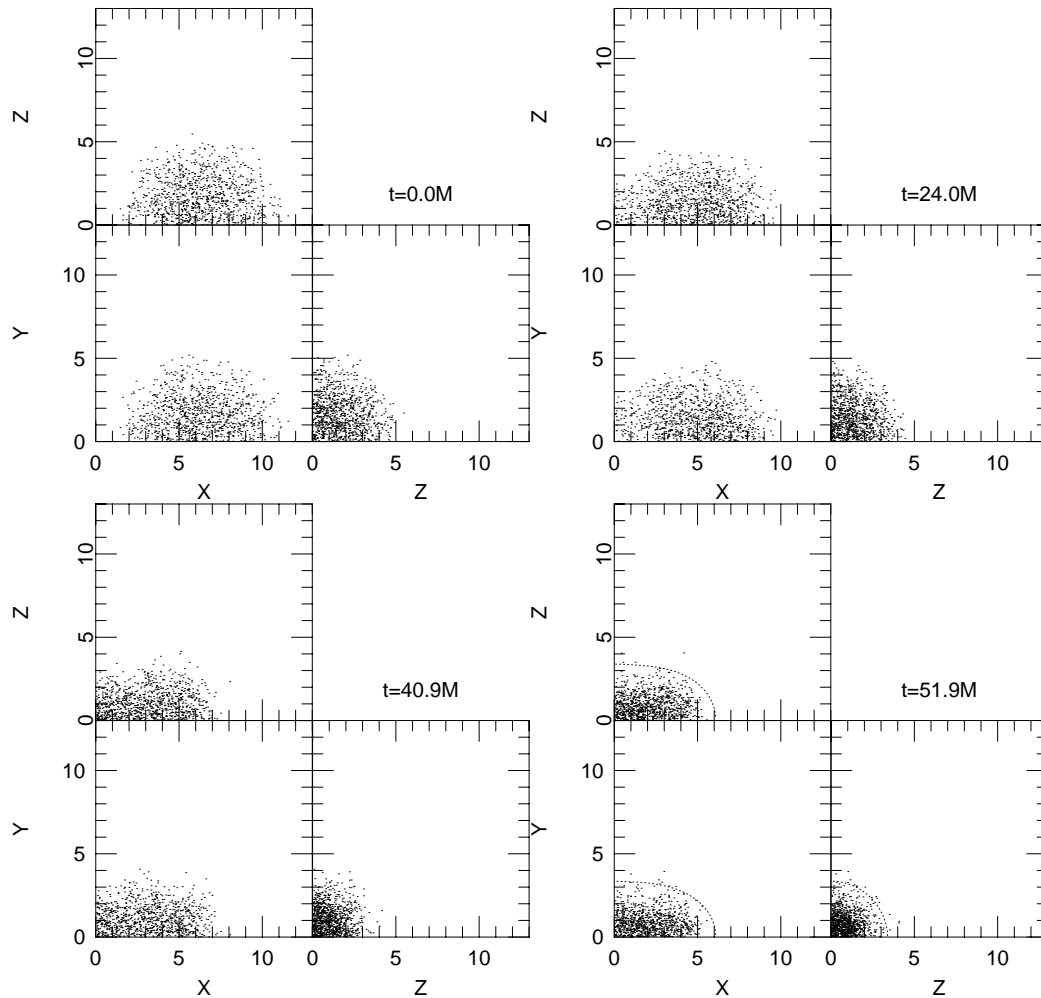

Fig. 13. The same as Fig. 7, but for a head-on collision of two clusters of initial boost velocity $a = 0.1M$, where M denotes half the mass of the system in these figures.

of Ω is not sufficiently large as in the case $\Omega = 1.2\sqrt{M/r_0^3}$, the centrifugal force of the ring cannot counteract its self-gravity, and its radius gradually decreases until it becomes a BH. On the other hand, if the initial value of Ω is sufficiently large, the ring settles down to a nearly equilibrium state due to a strong centrifugal force. It is noteworthy that the ring does not show any sign of non-axisymmetric instability up to the end of the simulations, and it appears to be stable against non-axisymmetric perturbations in these simulations. We guess that this may be due to the assumption of triplane symmetries. If we did not impose the symmetric condition, the ring might be unstable to fragmentation into several blobs.

8.3. *Head-on collision of two clusters*

We give numerical results for head-on collisions of two clusters in this subsection. As the initial conditions, we use two (nearly) equilibrium spherical clusters composed
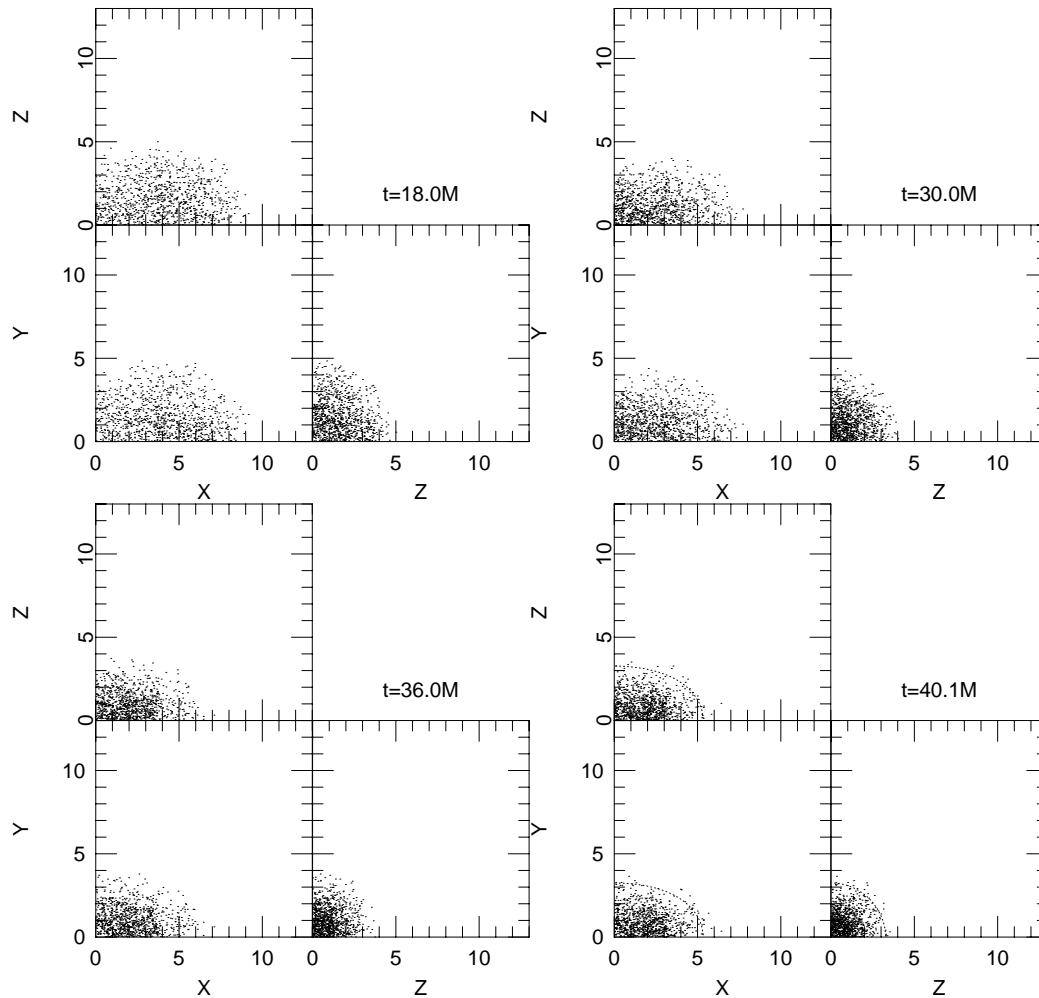

Fig. 14.   The same as Fig. 13, but for a head-on collision of two clusters of initial boost velocity $a = 0.3M$. Note that the particles positions at $t = 0$ are the same as those for the case $a = 0.1M$.

of equal numbers of co-rotating and counter-rotating particles as described in §7.2. The centers of clusters are located at $x = \pm 1.05 r_o$, where r_o is the radius of a cluster. We also add a uniform boost velocity, as described by Eq. (5·10), and use Eqs. (5·11) and (5·12) to give $\hat{A}_{ij}$. We first choose $r_o = 6 M_{\text{one}}$ as the coordinate radius of the equilibrium dust ball. Here, M_{one} denotes half the gravitational mass of the system (or in other words, the gravitational mass of one cluster).

In Figs. 13 and 14, we display snapshots of the particle positions at selected times for $a = 0.1 M_{\text{one}}$ ($M_* \simeq 1.088 M_{\text{one}}$) and $a = 0.3 M_{\text{one}}$ ($M_* \simeq 1.015 M_{\text{one}}$), respectively. It is found that each cluster is tidally deformed due to the gravity of the approaching companion, and as a result, the mean axial lengths of the y- and z-axes of each cluster are sufficiently small at the time of collision. Because of the tidal deformation, for the case in which the boost velocity is small ($a = 0.1 M_{\text{one}}$), a prolate object is first formed at the collision. Since there exists a boost velocity in the x-direction, the eccentricity of the prolate gradually becomes small, and finally a BH is formed at a time when the mean axial length of the x-axis is sufficiently small. For the case in which the boost velocity is large ($a = 0.3 M_{\text{one}}$), the mean axial lengths of the y- and z-axes of each cluster are not so small at the collision. Hence, the eccentricity of the merged object is not large at its formation, and a BH is quickly formed.

We also performed simulations fixing the radius of each cluster, the locations of center of clusters and the boost velocity, respectively, as $r_o = 6$, $x = \pm 6.3$, and $a = 0.1 r_6$, but changing the mass of each cluster to be $M_{\text{one}} = 0.5$, 0.3 and $0.25 r_6$ ($M_* \simeq 1.043$, 1.024 and $1.020 M_{\text{one}}$), where $r_6 \equiv r_o/6$. We find that for $M_{\text{one}} \geq 0.3 r_6$, a BH is formed after the collision, but otherwise it is not. Thus, the threshold of the total mass for BH formation is about $0.6 r_6$ (or $0.1 r_o$) for the initial density profile of the cluster we choose in this paper. One may think that the threshold of the mass is small compared with the single cluster case in which the threshold mass is $\sim 0.18 r_o$ (see §7.2). Hereafter, we consider the reason for this small threshold mass.

In Fig. 15, we show the time evolution of the mean axial length of the x- and y-axes. It is found that the mean axial length of the x-axis decreases at a constant rate due to the boost velocity. On the other hand, that of the y-axis (and z-axis) decreases due to the tidal force from the companion. At the collision ($t \sim 40$–$50 r_6$), the mean axial length of the y-axis becomes ~ 30–50% of the initial one. Thus, even if the compactness of each cluster is initially small, it is forced to become sufficiently large in the y- and z-directions at the collision. This clearly indicates that the pressure in the y- and z-directions initially given for one cluster of mass M_{one}
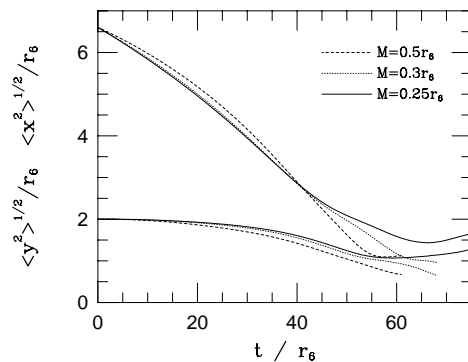

Fig. 15. Time evolution of $\langle x^2 \rangle^{1/2}$ and $\langle y^2 \rangle^{1/2}$ for head-on collisions of two clusters of each mass $M_{\text{one}} = 0.5$ (dotted lines), 0.3 (dashed lines) and $0.25 r_6$ (solid lines). (The total mass of the system is $2 M_{\text{one}}$.) Here, units of length, time and mass are $r_6 \equiv r_o/6$.

is too weak to support the merged object of mass $\sim 2M_{\mathrm{one}}$. This is the main reason that the threshold mass is small compared with that we expected.

In Fig. 16, we show snapshots of the particle positions at selected times for $M_{\mathrm{one}} = 0.25r_6$, where not a BH, but rather a new cluster is formed as a product of the collision. As mentioned above, up to the collision, y- and z-axes become sufficiently small due to the tidal force from the companion, and hence the merged object is very compact initially. However, the self-gravity is not sufficiently strong, so that the merged object bounces. Then, particles which have only small binding energies expand outward, while those which have large binding energies stay near origin. Finally, a new, nearly equilibrium cluster is formed. The formation process is essentially the same as that found in axisymmetric simulations by Shapiro and Teukolsky. [27]
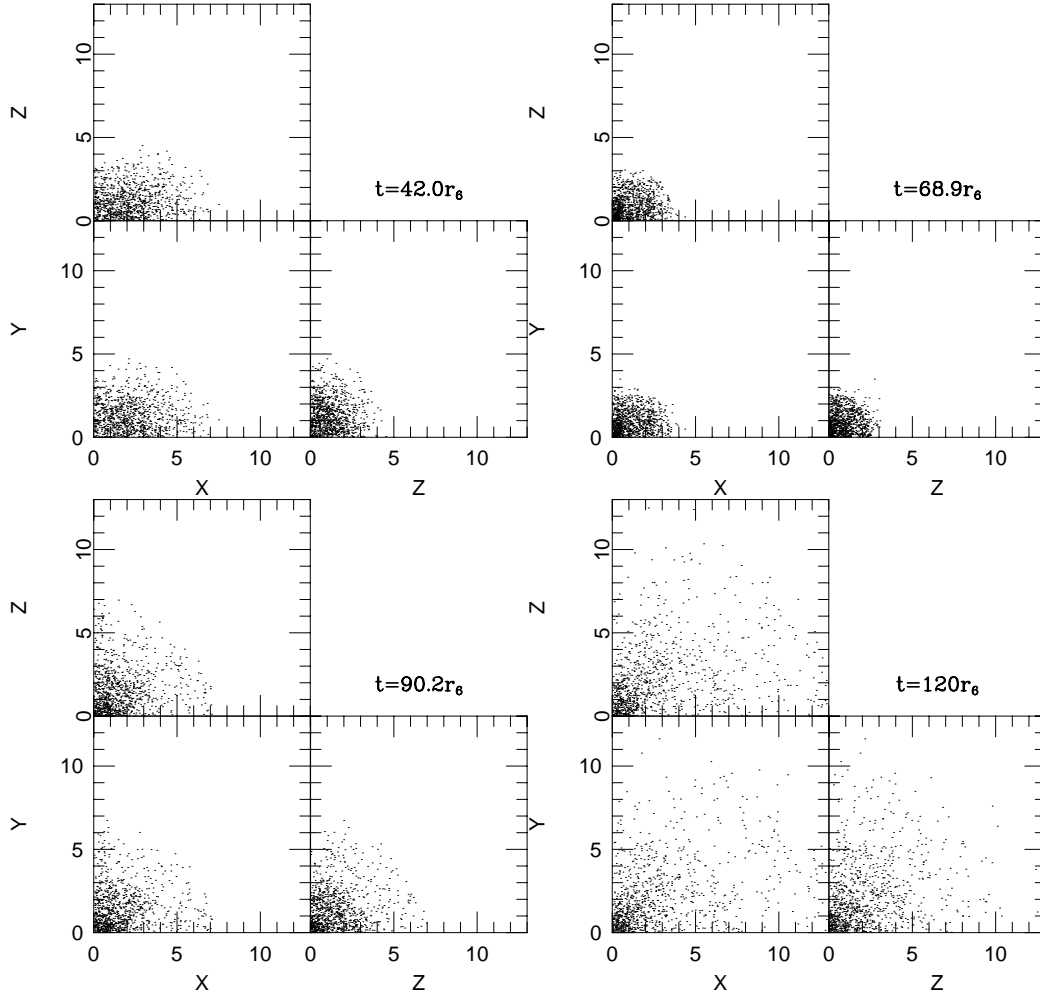

Fig. 16.   The same as Fig. 13, but for a head-on collision of two clusters of mass $M = 0.5r_6$ ($M_{\mathrm{one}} = 0.25r_6$). The particles positions at $t = 0$ are the same as those in Fig. 13.

§9. Discussion

We have performed a large variety of 3D numerical simulations for BH formation processes in triaxial symmetric spacetimes using a standard 3+1 formalism for the evolution of geometric variables and incorporating collisionless particles as a source of the energy momentum tensor and an apparent horizon finder. We chose an "approximate" maximal slice and zero shift vector conditions as the gauge condition. We have confirmed that our numerical scheme has the ability to investigate BH formation in triaxial gravitational collapse, collapse of spheroids of co-rotating and counter-rotating particles, and head-on collisions of two clusters fairly accurately.

Although numerical accuracy is maintained fairly well up to the formation of the apparent horizon, it becomes bad soon after the formation. This is simply because the gradients of geometric variables near the apparent horizon become very steep due to the so-called horizon stretching beyond the ability of numerical resolution. The main reason that we face the problem is that we use a time slice condition that possesses a singularity avoidance property. However, we believe that we must use the horizon avoiding slice at least up to the formation of the apparent horizon in order to determine the apparent horizon accurately. It therefore seems that horizon stretching cannot be avoided up to the formation of BHs in general.

As mentioned in §1, computation of gravitational waves is one of important goals in numerical relativity. To do this, numerical simulations have to be continued for a sufficiently long time up to the time at which gravitational waves reach the wave zone after the formation of the BH. Hence, it is necessary to resolve the horizon stretching problem using an implementation by which we can treat the horizon stretching region appropriately, such as an apparent horizon boundary condition. [28] For simulations after the formation of BHs, therefore, it is necessary to change the numerical code from our present scheme to another one.

It is also important to develop an extraction code for gravitational waves in the wave zone. In the simulations of head-on collisions of two clusters in this paper, a large fraction of gravitational radiation would be emitted, and the estimation of the amount is an important issue in numerical relativity. As wave extraction techniques, several methods have been proposed recently. [17] Incorporation of a wave extraction code is also one future issue.

Since we assume triplane symmetries in this paper, we cannot simulate the BH formation process for systems of finite total angular momentum such as a rotating collapse of a cluster and coalescence of two clusters. In order to investigate the effects of the angular momentum for formation processes of BHs, as the next step, we will perform such simulations changing our present numerical code to another one in which we assume π rotation symmetry along the z-axis. When we simulate a system of net angular momentum, we need to choose a spatial gauge condition carefully, because the shift vector plays an important role in reducing coordinate distortion in metric. We will suggest a new gauge condition and present numerical results by using it in a subsequent paper. [12]

Acknowledgements

References

1) A. Abramovici et al., Science **256** (1992), 325.
2) C. Bradaschia et al., Nucl. Instrum. and Methods **A289** (1990), 518.
3) J. Hough, in *Proceedings of the Sixth Marcel Grossmann Meeting*, ed. H. Sato and T. Nakamura (World Scientific, Singapore, 1992), p. 192.
4) K. Kuroda et al., in *Proceedings of International Conference on Gravitational Waves: Sources and Detectors*, ed. I. Ciufolini and F. Fidecaro (World Scientific, Singapore, 1997), p. 100.
5) For example, K. Oohara, T. Nakamura and M. Shibata, Prog. Theor. Phys. Suppl. No. 128 (1997), 183.
   E. Seidel, talk at 15-th meeting on General Relativity and Gravitation, Pune, India (1997).
   The Binary Black Hole "Grand Challenge" Alliance in Unite States, as for their recent efforts, see http://www.npac.syr.edu/projects/bh/.
6) M. Shibata and T. Nakamura, Phys. Rev. **D52** (1995), 5428.
7) M. Shibata, Phys. Rev. **D55** (1997), 2002.
8) S. L. Shapiro and S. A. Teukolsky, Philos. Trans. R. Soc. London **A340** (1992), 365, and references cited therein.
9) S. A. Teukolsky, Phys. Rev. **D26** (1982), 745.
10) C. W. Misner, K. S. Thorne and J. A. Wheeler, *Gravitation* (W. H. Freeman and Company, New York, 1973), p. 138.
11) L. Smarr and J. W. York, Jr., Phys. Rev. **D17** (1978), 1945, 2529.
12) M. Shibata, in preparation.
13) S. W. Hawking and G. F. R. Ellis, *The large scale structure of space-time* (Cambridge University Press, 1973).
14) R. W. Hockney and J. W. Eastwood, *Computer Simulation Using Particles* (Institute of Physics Publishing, Bristol and Philadelphia, 1988).
15) T. Nakamura, K. Oohara and Y. Kojima, Prog. Theor. Phys. Suppl. No. 90 (1987), 1.
16) For example, M. Shibata, T. W. Baumgarte and S. L. Shapiro, Phys. Rev. **D58** (1998), 023002.
17) For example, N. T. Bishop et al., gr-qc/9801070, and references cited therein.
   M. E. Rupright, A. M. Abrahams and L. Rezzolla, Phys. Rev. **D58** (1998), 044005.
   L. Rezzolla et al., gr-qc/9807047.
18) W. H. Press, B. P. Flannery, S. A. Teukolsky and W. T. Vetterling, *Numerical Recipes* (Cambridge University Press, 1989).
19) S. L. Shapiro and S. A. Teukolsky, Astrophys. J. **318** (1987), 542.
20) S. Chandrasekhar, *Ellipsoidal Figures of Equilibrium* (Yale University Press, New Haven, 1969).
21) S. L. Shapiro and S. A. Teukolsky, Astrophys. J. **298** (1985), 34.
22) M. Shibata, K. Nakao and T. Nakamura, Phys. Rev. **D50** (1994), 7304.
23) M. A. Scheel et al., Phys. Rev. **D58** (1998), 044020.
   T. W. Baumgarte and S. L. Shapiro, Phys. Rev. **D59** (1999), 024007.
24) A. M. Abrahams, S. L. Shapiro and S. A. Teukolsky, Phys. Rev. **D50** (1994), 7282.
25) S. L. Shapiro and S. A. Teukolsky, Phys. Rev. Lett. **66** (1991), 994.
26) R. M. Wald and V. Iyer, Phys. Rev. **D44** (1991), R3719.
27) S. L. Shapiro and S. A. Teukolsky, Phys. Rev. **D45** (1992), 2739.
28) E. Seidel and W.-M. Suen, Phys. Rev. Lett. **69** (1992), 1845.